Motivating a Synergistic Mixing-Layer Height Retrieval Method Using Backscatter Lidar Returns and Microwave-Radiometer Temperature Observations

Marcos P. Araújo da Silva⬛, *Graduate Student Member, IEEE*, Francesc Rocadenbosch⬛, *Senior Member, IEEE*, Robin L. Tanamachi⬛, and Umar Saeed

Abstract—Mixing-layer-height (MLH) retrieval methods using backscattered lidar signals from a ceilometer (Jenoptik CHM -15k Nimbus) and temperature profiles from a microwave radiometer (MWR) and Humidity And Temperature PROfiler (HATPRO) radiometer physics GmbH (RPG) are compared in terms of their complementary capabilities and associated uncertainties. The extended Kalman filter (EKF) is used for MLH retrieval from backscattered lidar signals, and the parcel method is used for MLH retrieval from MWR-derived potential-temperature profiles. The two principal sources of uncertainty in ceilometer-based MLH estimates are: 1) incorrect layer attribution (∼hundreds of meters) and 2) noise-induced errors (about 50 m at 3σ). MWR MLH uncertainties comprise: 1) the total uncertainty in the retrieved potential temperature profile and 2) ±0.5 K uncertainty in the surface temperature. Ceilometer- and MWR-based MLH estimates are, in turn, compared with reference to MLH estimates from radiosoundings. Twenty-one measurement days from the high definition clouds and precipitation for advancing climate prediction (HD(CP)^2) Observational Prototype Experiment (HOPE)

Manuscript received September 28, 2021; revised February 2, 2022; accepted February 21, 2022. Date of publication March 10, 2022; date of current version April 12, 2022. This work was supported in part by the Ministerio de Ciencia e Investigación (MCIN)/Agencia Estatal de Investigación (AEI)/10.13039/501100011033/FEDER under Project PGC2018-094132-B-I00 and Project MDM-2016-0600 (CommSensLab Excellence Unit) and in part by the European Commission collaborated under Project H2020 Aerosol, Clouds and Trace gases Research InfraStructure-IMplementation Project (ACTRIS-IMP) (GA-871115) and Project H2020 Sustainable ACESS to ATMOspheric Research Facilities (ATMO-ACCESS) (GA-101008004). The work of Marcos P. Araújo da Silva was supported in part by MCIN/AEI/10.13039/501100011033 under Grant PRE2018-086054 and in part by the European Social Fund (FSE) "El FSE invierte en tu futuro." *(Corresponding author: Francesc Rocadenbosch.)*

Marcos P. Araújo da Silva is with the CommSensLab-UPC, Department of Signal Theory and Communications, Universitat Politècnica de Catalunya (BarcelonaTech—UPC), 08034 Barcelona, Spain (e-mail: marcos.silva@upc.edu).

Francesc Rocadenbosch is with the CommSensLab-UPC, Department of Signal Theory and Communications, Universitat Politècnica de Catalunya (BarcelonaTech—UPC), 08034 Barcelona, Spain, and also with the Institute of Space Studies of Catalonia (IEEC), 08034 Barcelona, Spain (e-mail: roca@tsc.upc.edu).

Robin L. Tanamachi is with the Department of Earth, Atmospheric, and Planetary Sciences, Purdue University, West Lafayette, IN 47907 USA (e-mail: rtanamachi@purdue.edu).

Umar Saeed is with the Department of Communications and Networking, Aalto University, 00076 Espoo, Finland.

Digital Object Identifier 10.1109/TGRS.2022.3158401

campaign at Jülich, Germany, are considered. It is shown that the MWR can track the full mixed layer (ML) diurnal cycle (i.e., including morning and evening transitions) with height-increasing error bars. The ceilometer-EKF MLH estimates are much smaller errorbars than those from the MWR under the well-developed clear-sky ML, but the ceilometer-EKF is prone to ambiguous tracking some multilayer scenarios (e.g., the residual layer). We, therefore, introduce the synergistic MLH retrieval approach that combines both ceilometer and MWR estimates in order to optimize the benefits of both.

Index Terms—Atmospheric boundary layer (ABL) height, ceilometers, error analysis, laser radar, lidar, microwave radiometry, mixed layer (ML), remote sensing, signal processing.

I. INTRODUCTION

ACCURATE monitoring of the atmospheric boundary layer (ABL) is a subject of wide interest. The ABL, by definition, is directly affected by interactions with the surface of the Earth on a time scale of an hour or less [1], and it is also the layer of the atmosphere within which humans live. The mixed layer height (MLH) is a parameter of interest for many applications, including weather forecasting, air quality and chemical dispersion models, and aviation. In fair weather conditions, the interior of the ABL is well-mixed by convective turbulence (hence the term "mixed layer" or ML) and exhibits near-constant potential temperature (θ) and water vapor mixing ratio (r) throughout most of its depth. However, no remote or *in situ* instrument exists that can directly measure MLH. Instead, a proxy or tracer for the top of the ML must be used. Such tracers include gradients of aerosols, temperature, wind characteristics, or energy fluxes [2], [3]. Ground-based remote-sensing instruments that can detect these tracers include lidar, radar, and sonar, which are active and microwave radiometer (MWR), which is passive.

Because of the varying properties of these MLH tracers and estimation methods, their accuracy varies widely. Different studies have proven the reliability of MWR retrievals by comparison with radiosoundings. Radiosondes (RS), usually comprising an expendable, balloon-borne package of sensors, are a recognized reference instrument for boundary layer (BL) monitoring. Xu *et al.* [4] compared MWR-derived

temperature profiles averaged over a 30-min (full-span) window centered around the radiosonde profiles. Analyzing 403 (760) radiosonde launches from clear-sky (cloudy) days, they obtained correlation coefficients ≥ 0.85 up to ~ 7 km above ground level (AGL). Good agreement between MWR- and radiosonde-derived temperatures is also described by Löhnert and Maier [5], who reported differences lower than 0.5 K between the profiles up to 4-km AGL. In relation to MLH assessment, Collaud Coen et al. [6] applied the parcel method [7] to MWR- and radiosonde-retrieved θ profiles, obtaining median bias of -25.5 m and coefficient of determination $\rho^2 = 0.75$ ($\rho = 0.87$) over 100 samples. In a related study, Moreira et al. [8] found excellent agreement during convective conditions with a root mean square error (RMSE) = 190 m and $\rho = 0.96$.

The MWR has higher temporal resolution (e.g., a few minutes) than the radiosonde, whose operational frequency may be as low as two launches per day. However, its vertical resolution decreases with height, hence increasing uncertainty in retrieved quantities. In contrast, the lidar is an active remote sensing instrument designed to measure vertical profiles of aerosol backscattering with high spatiotemporal resolution. Aerosol concentrations are usually relatively high and constant throughout the ML and much lower aloft, thereby enabling lidar-based MLH estimation. In a fair-weather convective BL (CBL), MLH-lidar and MLH-MWR tend to converge. Belegante et al. [9] compared MLH estimates retrieved from elastic-lidar range-corrected-signal (RCS) profiles averaged over 30-min intervals with those from MWR-derived virtual potential temperature, finding high correlation ($\rho \approx 0.98$) in CBL conditions. However, during evening transition times (ETTs) (ETT; i.e., at and after sunset, when thermally driven turbulent mixing ceases), MLH-MWR is more accurate than MLH-lidar, which generally tended to track the residual layer (RL) (i.e., a remnant layer left over from earlier turbulent mixing) height [9]. Cimini et al. [10], using training data from multifrequency, multiangle MWR and lidar observations, designed a multivariate linear regression method to assess the mixing-layer height (MLH) directly from MWR brightness–temperature observations instead of retrieved profiles.

Lange et al. [11] (CommSensLab-UPC) estimated MLH by applying an extended Kalman filter (EKF) [12] to backscattered lidar returns (hereafter, MLH-LC-EKF). They showed that, for a CBL with moderate-to-low signal-to-noise ratio (SNR > 5), MLH-LC-EKF was more accurate than classical approaches, such as the threshold [13], gradient [14], logarithmic gradient [15], inflection point [16], and variance methods [17]. In addition, Banks et al. [18] showed the MLH-LC-EKF reliability against radiosonde-derived Bulk Richardson Number profiles and against weather research and forecasting (WRF) model predictions for clear-air and preconvective storm cases. Based upon these works, Moreira et al. [8] found correlated results among MLH estimates in the CBL derived from LC-EKF, MWR, and Doppler wind lidar (DWL) combinations. The EKF has also been used as an MLH retrieval method when applied to S-band radar returns [19], [20]. In a different context,

TABLE I
LIST OF ACRONYMS AND ABBREVIATIONS USED THROUGHOUT THIS MANUSCRIPT

Acronym	Definition	Reference(s)
ABL	Atmospheric boundary layer	[1]
CBL	Convective boundary layer	[1]
ML	(Well-)mixed layer	[1]
FT	Free troposphere	[1]
EZ	Entrainment zone	[1]
RL	Residual layer	[1]
MLH	Mixed layer height	[1]
CBH	Cloud base height	[24]
MTT	Morning transition time	[1]
ETT	Evening transition time	[1]
JOYCE	Jülich ObservatorY for Cloud Evolution	[25]
HOPE	HD(CP)^2 Observational Prototype Experiment	[23]
MWR	Microwave radiometer	[25], [26]
LC	Lidar ceilometer	[24]
DWL	Doppler wind lidar	[26], [27]
RS	Radiosonde	[28]–[30]
EKF	Extended Kalman filter	[12]
VVSTD	Vertical Velocity Standard Deviation	[27], [31]
MLH-MWR	MLH estimated by application of the parcel method to MWR measurements	[3], [7]
MLH-LC-EKF	MLH estimated by application of the EKF method to LC measurements	[11], [19]
MLH-DWL	MLH estimated by application of the VVSTD method to DWL measurements	[27]
MLH-RS	MLH estimated by application of the parcel method to RS measurements	[3], [7]
SYN	Synergistic method optimally combining MLH-MWR and MLH-LC-EKF	This manuscript
MLH-SYN	MLH estimated by the SYN method	This manuscript

Barrera-Verdejo et al., [21] combined brightness–temperature information from an MWR and water-vapor mixing-ratio Raman lidar profiles in order to derive absolute humidity vertical profiles.

Most of the previous work done for ML retrieval using backscattered lidar signals or temperature profiles has been focused on "stand-alone" retrieval methods only. However, tentative derivation of a synergistic algorithm spanning the full diurnal cycle and the study of the uncertainty sources associated with MLH estimation and their statistical impact on the retrievals has not received much attention [22].

To fill this void, this article focuses on synergistic retrieval of MLH estimates with low uncertainty by combining ceilometer and MWR MLH-based retrievals using the EKF and the parcel method as respective estimators. Toward this end, this article aims to study: 1) the performance of these two commonly used algorithms under different atmospheric scenarios; 2) the impact of key error sources, namely, measurement and retrieval errors, on MLH estimates; and 3) evaluate the performance of the proposed synergistic ceilometer-MWR method. The simplified processing chain of the ceilometer and MWR data is summarized in Fig. 1.

This article is organized as follows. Section II introduces instruments and datasets. Section III revisits the proposed MLH estimation methods and related error sources, assesses their uncertainties on the MLH estimates via error propaga-
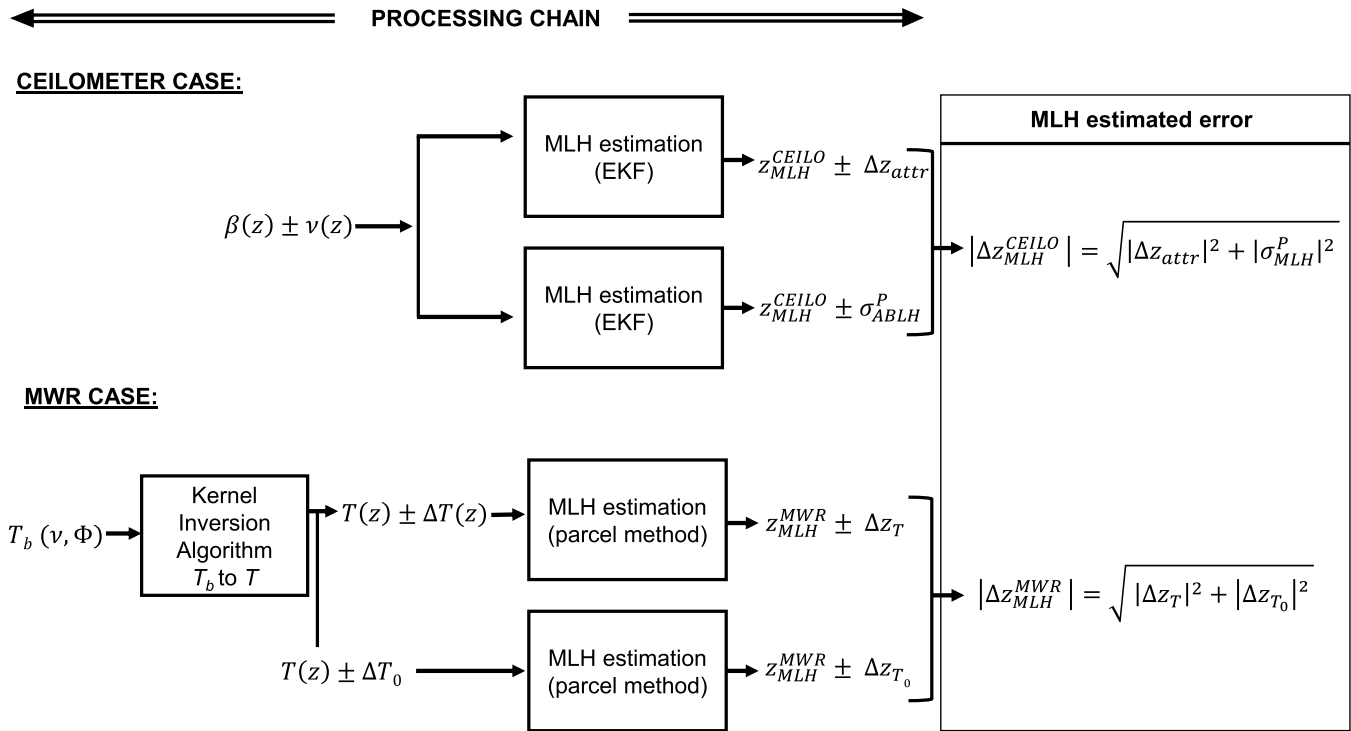
PROCESSING CHAIN

Fig. 1. Block diagram illustrating the ceilometer (top) and MWR (bottom) processing chains used to estimate the mixing-layer height (MLH) and related error estimates. z is the vertical coordinate (height). $\beta(z)$ is the attenuated backscatter, $\nu(z)$ is the related corrupting noise, z_{MLH}^{CEILO} is MLH-LC-EKF, Δz_{attr} is the uncertainty of MLH-LC-EKF due to incorrect layer attribution, and σ_{MLH}^{P} is the MLH error component due to noise. $T_b(\nu, \phi)$ is the MWR brightness temperature measured at frequency ν and elevation angle ϕ, $T(z)$ is the retrieved temperature profile, Δz_T is the MLH-MWR error component due to the total uncertainty of $T(z)$, and Δz_{T_0} is the MLH-MWR error component due to uncertainty in the auxiliary measured surface temperature T_0. Δz_{MLH}^{CEILO} and Δz_{MLH}^{MWR} stand for the total estimated errors for MLH-LC-EKF and MLH-MWR, respectively.

tion from both ceilometer- and MWR-based methods, and introduces the synergistic method (SYN). Section IV presents statistical analysis and discussion of results based on 20 days selected from the high definition clouds and precipitation for advancing climate prediction (HD(CP)^2) Observational Prototype Experiment (HOPE) [23] campaign. Finally, Section V gives concluding remarks.

Due to the various combinations of BL terminology, instruments, and methods used in this article, we provide an acronym table for ease of reference (see Table I).

II. INSTRUMENTS AND DATASET

Data used in this work was collected at the Jülich ObservatorY for Cloud Evolution (JOYCE), which is located in Forschungszentrum, Jülich, Germany [50°54′31″ N, 6°24′49″ E, 111-m mean sea level (MSL)]. The topography in the area of JOYCE is generally flat apart from large lignite open-pit mines. Farming, open-cast coal mining areas with major power plants and patchy settlements characterized the 50-km periphery. The climate is characterized by a temperate, humid climate with warm summers [25]. JOYCE contains a number of active and passive permanently installed remote sensing, and *in situ* instruments aimed to the study of clouds and atmosphere. The HOPE campaign [23] was conducted at JOYCE from April 2013 to May 2013. One of the principal aims of HOPE was to characterize the evolution of the ABL over JOYCE for forecasting applications. We chose to examine the data

from this campaign because they contain long-duration, simultaneous observation of MLH tracers by multiple independent instruments, a situation ideal for validation. For brevity, only those JOYCE instruments used in HOPE are described in the following. The reader is referred to [25], [32] for a complete listing.

A. Ceilometer

A lidar ceilometer is a single-wavelength elastic-backscatter lidar characterized by a low energy-aperture product. Under moderate-to-clear-air atmospheres (optical thickness, $\tau < 1$) and, particularly, toward the near-infrared, the profile of the attenuated-backscatter coefficient is essentially proportional to the aerosol concentration in the ABL [11], [24], [27].

Two LCs are used in this work. The first is a Jenoptik CHM-15k Nimbus, an $8 - \mu$J, 1064-nm wavelength, 5-ns-pulse duration, and 5-to-7-kHz repetition-rate ceilometer. Under clear-sky conditions, the maximum sounding range is about 15 km with a range resolution of 15 m. The temporal resolution of the instrument is 15 s. The Jenoptik ceilometer is a biaxial system with separate optics for the transmitter and receiver so that the optical overlap is reached at about 350 m. The instrument provides range- and overlap-corrected profiles of the normalized backscattered power (i.e., the attenuated backscatter-coefficient profile).

The second LC used in the HOPE campaign was a Vaisala CT25K used to monitor cloud-base height (CBH) and precipitation and to complement Jenoptik's observations

below 350 m (night-time and morning/afternoon transition periods). The Vaisala CT25K is a $1.6 - \mu$J, 905-nm wavelength, 100-ns pulse duration, and 5.6-kHz repetition-rate LC designed to retrieve profiles of the attenuated-backscatter coefficient in the sounding range from 60 m to 7 km, with a range resolution of approximately 30 m. The temporal resolution of the instrument is 15 s (including 3.3 s for processing and data transmission). Because of the lower pulse energy of the Vaisala LC compared to the Jenoptik (and because both systems operate in similar, near-infrared wavelengths), Jenoptik's vertical profiles of the attenuated backscatter coefficient exhibit a comparatively high SNR.

B. MWR: Humidity And Temperature PROfiler (HATPRO)

An MWR measures the radiative emission of atmospheric gases. The emissions from molecular oxygen, in particular, are proportional to atmospheric temperature when the water vapor mixing ratio remains constant. Measurements at different frequency bands and elevation angles can be used to derive several physical quantities, such as temperature, water vapor, integrated water vapor, and liquid water path. The Humidity And Temperature PROfiler (HATPRO) MWR manufactured by radiometer physics GmbH (RPG) [25], [26] measures the atmospheric brightness temperature at 14 frequencies in two bands and at six angles (depending on user's settings). Measurements in the K-band (seven channels), 22–31 GHz, are used for water vapor and liquid water retrieval, and in the V-band, 51–58 GHz, for temperature retrieval. The MWR instrument exhibits good temporal resolution (about 2.7 min). In principle, MWR can operate in all conditions except for rain when the radiation measured is dominated by the emission and scattering from raindrops.

Brightness–temperature measurements are converted into a temperature profile by means of a statistical retrieval algorithm [33]–[36] together with auxiliary atmospheric temperature and pressure data. The latter is measured separately by surface-based *in situ* sensors. Ultimately, the retrieved potential temperature profile is used to estimate the MLH. In this formulation, two main error sources are delineated: 1) MLH estimation errors, Δz_T, originating as a total uncertainty in the retrieved temperature profile ($\Delta T(z)$ in Fig. 1) and 2) MLH errors due to uncertainties in the auxiliary measurement of surface temperature, Δz_{T_0}. MLH estimates and related errors are computed according to the different spatial resolutions of each instrument. The MWR-derived temperature profile exhibits a coarse ($\geq$50 m) vertical resolution that increases with height [5], [35], which is specific to the retrieval algorithm and to the number of measurement channels (sounding frequencies) being used. Because the number of independent pieces of information contained in the brightness temperature measurements at different frequencies and scanning angles is limited, the resulting Degree of Freedom (DoF) is low (≈ 4 for temperature BL profiling) [5]. As a result, the vertical resolution of the retrieved quantities substantially decreases (i.e., becomes coarser) with height. As a general rule, the vertical resolution is approximately equal to the height above the surface. For example, the vertical resolution at 1-km

AGL is roughly 1 km (i.e., the retrieved temperature at 1-km AGL is valid for the 500–1500-m layer).

C. Doppler Wind Lidar

Because the free troposphere (FT) is generally not as turbulent as the ML, vertical gradients in the standard deviation (STD) of velocity can be used as a tracer of the MLH [31], [37]. A DWL indirectly measures the ABL mixing process via vertical wind velocity variance [26], [27]. Driven by the technological progress in the wind energy industry in the last couple of decades, economical and useful DWL systems have been developed [38].

The DWL used in the HOPE campaign is the HALO Photonics Streamline Wind Lidar [27], [38], [39], a coherent system with an average pulse energy of 100 μJ and a frequency of 15 kHz. The vertical resolution of this system is 30 m, and the maximum range is about 8 km. However, in practice, its effective maximum range becomes limited by the reduced aerosol content above the ABL.

D. Radiosonde

The Radiosonde is a *de facto* standard for reference in the atmospheric sciences [28]–[30]. Radiosondes measure *in situ* profiles of the atmospheric thermodynamic state (temperature, pressure, water vapor, and wind) and are usually launched attached to a large balloon. A radiosonde can rise up to 40 km in height over the course of several hours, though most water-vapor sensors usually cease to operate properly below the tropopause ($\sim$15 km in the midlatitudes).

The radiosonde used in this work is the Graw DFM-09 manufactured by Graw GmbH, which includes temperature, pressure, humidity, and Global Positioning System (GPS) sensors (20 channels). Wind speed and direction are determined from the changes in the GPS position and GPS velocity vector. The transmission rate is one full set of observations per second. The main drawbacks of using radiosondes for MLH determinations are the sparse temporal resolution (due to the expense associated with each launch) and horizontal drift on the ascent. During the HOPE campaign, 226 soundings were launched up to a maximum of six per day (07:00, 09:00, 11:00, 13:00, 15:00, and 17:00 UTC; local time, LT=UTC+1 h) from a site located 3.8-km southeast of JOYCE.

III. METHODS AND UNCERTAINTIES OF MLH ESTIMATION

When comparing ceilometers and MWRs, the instruments at the focus of this article, ceilometers, typically have higher vertical resolution (e.g., 15 m for the Jenoptik CHM-15k Nimbus ceilometer versus 50 m or greater for the MWR). Because the ceilometer relies on attenuated backscatter returns from atmospheric aerosols and molecules, which are proxies of the thermodynamic state of the atmosphere, to identify the MLH, layer-attribution problems are very common. On the other hand, MWR-derived temperature profiles have a much coarser vertical resolution than profiles from LCs

(see Section II). In addition, parcel method-based MLH estimates suffer from uncertainties associated with surface temperature Δz_{T_0}. We now explore these sources of uncertainty in greater detail.

A. MLH Estimation From Ceilometer Data

MLH Estimation Method: Several classical methods for LC-based MLH estimation, such as the gradient method [14], [40], the inflection-point method [16], and the variance method [17], among others [13], [41], are based on the detection of a meaningful ML-to-FT sharp transition in the vertical profile of the attenuated backscatter coefficient. However, thermal updrafts, intermittent turbulence, and measurement noise often lead to time-inconsistent MLH retrievals even in single aerosol layer scenarios. Apart from noise, these fluctuations represent real physical processes in the atmosphere, but they can complicate MLH tracking. To counteract detrimental effects of these fluctuations on MLH tracking, backscatter profiles are often time and/or height averaged [11]. Therefore, temporal resolution of LC-based MLH estimates is usually relatively low (∼30 min). LC-based algorithms for MLH estimation (in convective and stable regimes) in recent literature [6], [42], [43] use time-continuity and morphological criteria based on a combination of empirically tuned gradient and variance criteria, signal and SNR conditions, and climatological data.

In this study, we apply the EKF MLH estimation method [11], [19], which departs from previous works of [44], using a time-adaptive, optimal predictive model to delineate the shape of the sharp ML-to-FT transition [see Fig. 2(a)]. The Kalman filter is essentially the Wiener solution [45] of the optimal filter problem in which one wants to compute a statistical estimate of an unknown signal (the MLH as a function of time) using a related signal (i.e., the ceilometer attenuated backscatter height profile as a function of time) to produce the estimate as an output. The two main distinguishing features of the Kalman filter formulation are: 1) vector modeling of the random processes under study (i.e., the MLH and shape parameters defining the ML-to-FT transition as a function of time) and 2) recursive processing of the input noisy measurements (the ceilometer's) at each successive discrete time. This time-adaptive behavior of the filter is based on minimization of the mean squared error over time of the so-called *a posteriori* error covariance matrix (the term *a posteriori* meaning "once the filter is updated with the present-time measurement," i.e., from the ceilometer). The reader is referred to [11], [19] for a complete derivation of the EKF-based method for MLH tracking in LC data (hereafter, MLH-LC-EKF), particularly Appendix A of [11] for a summary of the filter's constitutive equations and proof of its optimality. In Section III-A1 the MLH-LC-EKF is briefly summarized for self-contained purposes and notation definition.

As a result, MLH-LC-EKF [11] enables consistent time-tracking of the MLH without the need of averaging techniques or training from ancillary climatological records. Because the filter estimates are generated at the same temporal and spatial resolutions of the input measurement data, the filter can even be implemented as a real-time processor. The
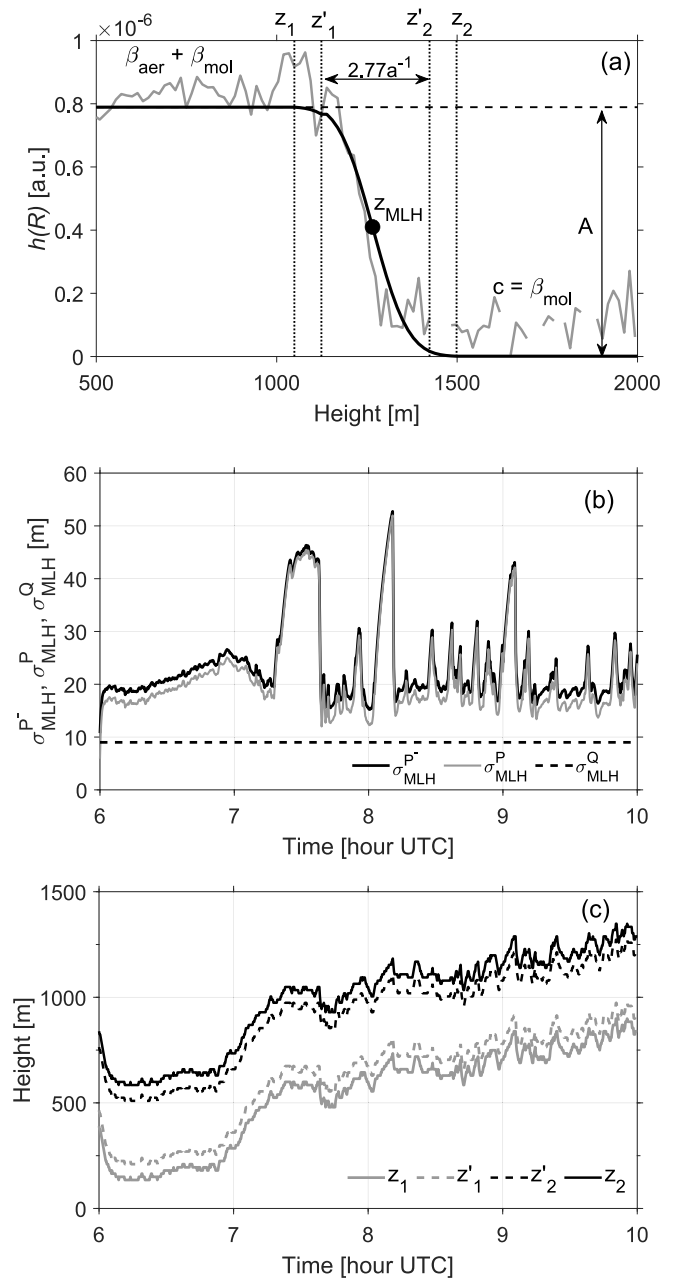
Fig. 2. Example of the MLH-LC-EKF estimation technique (April 20, 2013, 0600–1000 UTC). (a) ML-to-FT transition model. (Gray trace) Example of background-subtracted attenuated backscatter-coefficient profile measured by the LC. (Black curve) Fit erf-model profile described in [11]. (b) MLH-LC-EKF *a priori* error, $\sigma_{\text{MLH}}^{P^-}$, *a posteriori* error, σ_{MLH}^{P}, and state-noise STD, σ_{MLH}^{Q}, as a function of time. (c) Temporal evolution of search boundaries z_1, z_1', z_2', and z_2.

best performance of the EKF with reference to the classical methods above has been shown in [11], [18], [46] with reference to different parameterizations of the WRF model.

1) Review of the MLH-LC-EKF: Central to the MLH-LC-EKF method is the assumption of the erf-like ML-to-FT model

$$h(z; z_{\text{MLH}}, a, A, c) = \frac{A}{2}\left\{1 - \text{erf}\left[\frac{a}{\sqrt{2}}(z - z_{\text{MLH}})\right]\right\} + c \quad (1)$$

where z_{MLH} is the MLH, a is a scaling factor related to the entrainment zone (EZ) thickness ($2.77a^{-1}$) [31], [40], A is

the total backscatter coefficient, and c is the FT molecular backscatter background, which acts as an offset term to the filter.

The erf model depicted in Fig. 2(a) models the ML-to-FT transition of the attenuated backscatter coefficient measured by the ceilometer. This model is used as a proxy of the total atmospheric backscatter coefficient under the assumption of clear-to-moderately cloudy sky conditions (optical thickness, $\tau < 1$). The shape parameters of this model profile along with the MLH parameter itself give rise to the formulation of the state vector (to be estimated)

$$x_k = [z_{\mathrm{MLH},k}, a_k, A_k, c_k]^T \tag{2}$$

where subscript k is a discrete time. $z_{\mathrm{MLH},k}$ is the key parameter of interest, and a_k, A_k, and c_k are auxiliary parameters determining the change in shape of the ML-to-FT interface with time.

The *state-vector model* represents the transition of the state vector from time t_k to t_{k+1}. It is formulated as

$$x_{k+1} = x_k + w_k \tag{3}$$

where w_k is the state-noise vector with diagonal covariance matrix and $Q_k = E[w_k w_k^T]$, where E denotes the ensemble mean (or expectation) operator [47]. For enhanced filter stability [48], Q_k is modeled in stationary diagonal form as $Q = \mathrm{diag}[\sigma_Q^2]$, $\sigma_Q = [\sigma_{z_{\mathrm{MLH}}}, \sigma_a, \sigma_A, \sigma_c]$, where $\sigma_{z_{\mathrm{MLH}}}, \sigma_a, \sigma_A$, and σ_c are the guessed STDs associated with the state-vector components, z_{MLH}, a, A, and c, respectively. For example, $\sigma_{z_{\mathrm{MLH}}}$ models the STD of the MLH (a random variable) around its mean value. In practice, for simplicity, the input vector σ_Q is constructed as

$$\sigma_Q = \mu_Q \hat{x}_0^- \tag{4}$$

where μ_Q is the so-called Q-intensity factor (a scalar) and $\hat{x}_0^-$ denotes the initial guess of the state vector at filter startup to be specified by the user. In what follows, we have used $\mu_Q = 0.1$ (10%). This means that, if we assume an initialization $z_{\mathrm{MLH},0} = 1500$ m, then we expect MLH fluctuations of approximately ± 150 m (10%) at 1σ. Because the state vector is recursively recomputed at each filter step, an intensity factor $\mu_Q = 0.1$ is usually more than sufficient to search the full ML height span. Increasing this factor above 10% increases the search "nervousness" of the filter. This effect is usually not beneficial because it may lead the filter to jump between different aerosol layers and, hence, be more prone to divergence. The initial guess vector $\hat{x}_0^-$ can easily be estimated by plotting the erf model against one measured ceilometer attenuated backscatter profile, as shown in Fig. 2(a).

The *measurement model* relates the ceilometer measurement vector, y_k, to the state vector as

$$y_k = h(x_k) + v_k \tag{5}$$

where h is the erf-like ML-to-FT function model given by 5 above, v_k is the observation noise at time t_k with noise covariance matrix, $R_k = E[v_k v_k^T]$, and z is the vertical range. The measurement vector, $y_k = (y_{1,k}, y_{2,k}, \ldots, y_{N,k})$, is the noise-corrupted ceilometer attenuated backscatter signal

at discrete ranges, $z = z_i, i = 1, \ldots, N$. Because there is only one single measurement realization available at each time t_k, the instantaneous noise covariance matrix R_k is estimated in piecewise form over range cells instead of time cells, as described in [19], (19). The nonlinear model of 5 is linearized through its Jacobian, which is passed to the filter.

2) Error Sources: There are two key sources of uncertainty concerning MLH estimation from ceilometer data: 1) layer-attribution errors and 2) noise-induced errors.

(i) Impact of Layer-Attribution Errors on the Estimated MLH, Δz_{attr}: Layer-attribution errors arise from the existence of multiple layers or gradients in the attenuated backscatter profile. Depending upon the number of layers and their separation, the estimated MLH can be significantly different from the actual MLH. For example, during the ETT (ETT; also called the afternoon-to-evening transition or AET, see [49]) under quiescent conditions, the ML is replaced by the RL [1]. In this case, it often happens that the MLH-LC-EKF estimate follows the RL because RL-to-FT aerosol gradient characteristics are similar to those of the ML top [50], particularly in the 1–2-h period following local sunset. Provision of acceptable initial guesses for the state vector, $\hat{x}_0^-$, state-vector covariance, Q, and *a priori* state-vector error covariance matrix, P_0^-, are key to preventing layer-attribution errors. This is especially true during the morning transition time (MTT) (MTT, i.e., at and after local sunrise), when the ML starts to develop and there are relatively steep backscatter aerosol gradients between the ML and the RL or FT above. An example of this phenomenon is illustrated in Fig. 3(a). Previous work on assessing the uncertainty of the MLH estimate due to layer-attribution errors has been carried out by [50].

The *a priori* and *a posteriori* error-covariance matrices are defined as

$$P_k^- = E[e_k^- e_k^{-T}], \quad P_k = E[e_k e_k^T] \tag{6}$$

respectively, where $e_k^- = x_k - \hat{x}_k^-$ is the *a priori* error and $e_k = x_k - \hat{x}_k$ is the *a posteriori* error, i.e., before and after assimilating the current measurement (y_k). Here, x_k is the true atmospheric state (unknown), and $\hat{x}_k^-$ and $\hat{x}_k$ are the *a priori* and *a posteriori* state vectors estimated by the filter, respectively.

Covariance matrices P_k^- and P_k are updated with each successive step of the recursive loop of the filter [see Fig. 2(b)] as a function of the current information available to the filter at time t_k (actual Kalman or projection gain, K_k, linearized Jacobian, state vector, x_k, state-vector covariance matrix, P_k, and measurement-noise covariance matrix, R_k) and initial settings at t_0. The initial guess of the *a priori* state-vector error covariance matrix, P_0^-, is a rough estimate of the uncertainty associated with the initial guess of the state vector, $\hat{x}_0^-$, in the form of a diagonal matrix $P_0^- = \mathrm{diag}[\sigma_P^2]$, $\sigma_P = (\sigma_{e,z_{\mathrm{MLH}}}, \sigma_{e,a}, \sigma_{e,A}, \sigma_{e,c})$, where $\sigma_{e,X}$, $X = [z_{\mathrm{MLH}}, a, A, c]$ represents the assumed uncertainty of the initial guess and $\hat{x}_0^- = [z_{\mathrm{MLH},0}, a_0, A_0, c_0]^T$ at 1σ level. σ_P is shorthand notation for $\sigma_{P_0^-}$. We compute the input vector σ_P as

$$\sigma_P = \mu_P \hat{x}_0^- \tag{7}$$
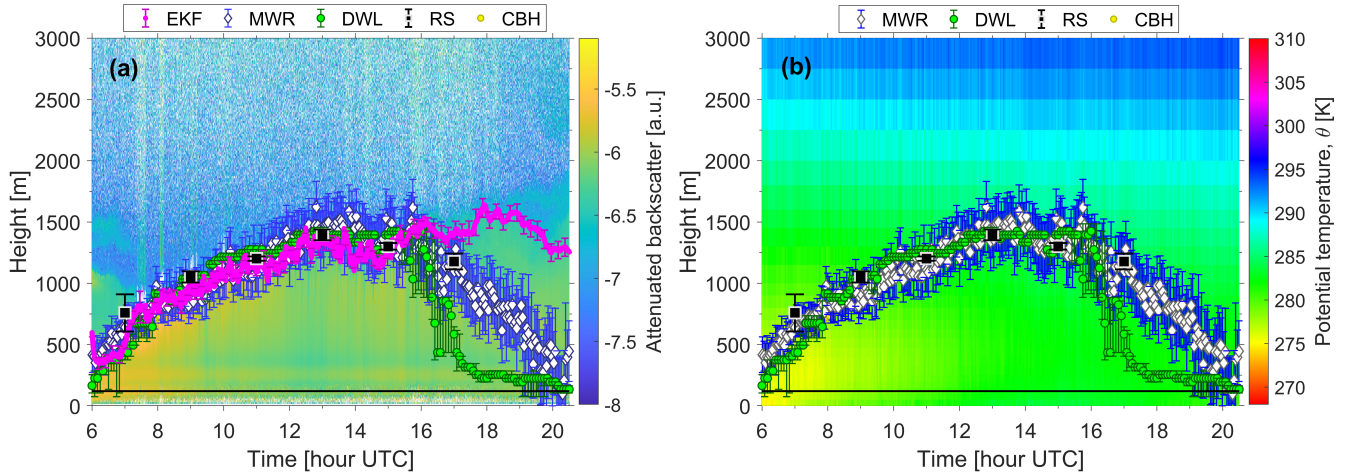
Fig. 3. (a) Attenuated ceilometer backscatter (in a.u.) measured by the Jenoptik CHM-15 and (b) MWR-retrieved potential temperature (in K) for 20 April 2013 at Jülich, Germany. In panel (a), magenta dots (along with noise-related error bars) represent MLH-LC-EKF. In both panels, white diamonds represent MLH-MWR with associated uncertainty $\Delta z_{\text{MLH}}^{\text{MWR}}$ (blue error bars); black squares are MLH-RS; green dots MLH-DWL; and yellow dots are CBH estimates from the Vaisala CT25. In both panels, the solid black line represents a lower bound (120 m) on MLH-DWL.

where μ_P denotes the P-intensity factor to be specified by the user. Factors in the range $\mu_P = 0.1$–$0.3(10\%$–$30\%)$ have been used in the examples of Section IV with $\mu_P = 0.3$ the default setting. High/low values $(0.3/0.1)$ tend to increase/decrease the search span of the filter during the first iterations. For example, assuming that $z_{\text{MLH},0} = 1500$ m, the setting $\mu_P = 0.3$ tells the filter that the user expects the MLH to be roughly at 1500 ± 450 m at filter startup. P- and Q-intensity factors are partially coupled parameters because of the recursive nature of the filter, and therefore, the guidelines above are just orientative. Layer-attribution errors are common because, irrespective of the user's initializations for $\hat{x}_0^-$ and σ_P, successful filter operation is always conditioned to the existence of aerosol gradients. Therefore, Δz_{attr} can only be known by comparison to a reference instrument (e.g., the radiosonde).

(ii) Impact of Observation Noise and Resulting a Posteriori Error on the Estimated MLH, σ_{MLH}^P: Noise-induced errors are due to the presence of noise in $\beta'(z)$ and propagate an error to the MLH-LC-EKF estimate. The recursive loop of the EKF provides by itself convenient error estimates $(\boldsymbol{P}_k^-, \boldsymbol{P}_k,$ and $\boldsymbol{Q}_k)$ of the estimated state vector and, therefore, of the estimated MLH at each discrete time t_k.

Fig. 2(b) shows the estimated *a priori* and *a posteriori* errors for the case shown in Fig. 3 computed as the time-dependent STDs, $\sigma_{\text{MLH},k}^{P^-}$ and $\sigma_{\text{MLH},k}^{P}$, respectively. These are compared to the time-static state noise STD, σ_{MLH}^{Q}. STDs $\sigma_{\text{MLH},k}^{P^-}$, $\sigma_{\text{MLH},k}^{P}$, and σ_{MLH}^{Q} are computed as the square root of the first diagonal element of these matrices during the recursive loop of the filter. The error of the instantaneous MLH-LC-EKF estimate at time t_k is given by the *a posteriori* error as

$$\sigma_{\text{MLH},k}^{\text{EKF}} = \sigma_{\text{MLH},k}^{P} \qquad (8)$$

which is the key error indicator of interest. In Fig. 2(b), it can be seen that the *a posteriori* error magnitude, $\sigma_{\text{MLH},k}^{P}$, is always smaller than the *a priori* error, $\sigma_{\text{MLH},k}^{P^-}$. This variance reduction, $\left(\sigma_{\text{MLH},k}^{P}\right)^2 < \left(\sigma_{\text{MLH},k}^{P^-}\right)^2$, means that the assimilation of the

present measurement $\boldsymbol{y}_k$ counteracts the detrimental effects of observation noise. The latter term merges into a single body both measurement noise $\upsilon(z)$ (with $\boldsymbol{R}_k$ being estimated run time) and modeling noise (i.e., approximation of the ML-to-FT transition by the erf model used in MLH-LC-EKF). $\sigma_{\text{MLH},k}^{Q}$ is just a reference baseline of the user's assumed MLH variability. Fig. 2(c) depicts time evolution of search boundaries z_1, z_1', z_2', and z_2 [see Fig. 2(a)] during the first four hours of data processing [11].

The error estimates above are obviously subordinated to filter convergence and tracking of the ML-to-FT interface (i.e., no attribution errors). Otherwise, the total error from sources 1) and 2) above can be calculated by using the error superposition principle as (see Fig. 1)

$$\left|\Delta z_{\text{MLH}}^{\text{CEILO}}\right| = \sqrt{\left|\Delta z_{\text{attr}}\right|^2 + \left|\sigma_{\text{MLH}}^{P}\right|^2}. \qquad (9)$$

B. MLH Estimation From DWL Data

To estimate the MLH from DWL measurements, the STD of time-height profiles of vertical velocity are calculated every 5 min within a ± 15 min window. Second, the STD is corrected for instrument noise [51]. Finally, the MLH is estimated as the first height at which the Vertical Velocity STandard Deviation (VVSTD) falls below a predetermined threshold [27], [52], [53] (hereafter, MLH-DWL).

Useable thresholds for VVSTD range from 0.2 to 0.4 m·s^{-1} [52], [53]. Based on the work of [27], who studied the sensitivity of the mixing layer height derived from different thresholds, here, we use a 0.4-m·s^{-1} threshold. Because 0.4 m·s^{-1} is at the high end of the accepted range, it represents a major source of uncertainty.

DWL-based estimates of ML height (MLH-DWL) are generally limited to daytime hours when the BL is turbulent due to solar heating and thermally driven ML overturn. MLH-DWLs at night are less reliable because aerosol content is reduced in stable situations at night. In addition, mixing layer height

values below 120 m AGL are rejected as the DWL is not sufficiently sensitive below this height.

The uncertainty associated with the DWL-derived MLH is estimated by applying a 25% variation to the nominal threshold (th$_\pm$ = 0.4 m·s^{-1} ±0.1 m·s^{-1}) [27]. Upper and lower uncertainty bounds are derived from the MLH estimations using 0.5- and 0.3-m·s^{-1} thresholds, respectively, minus the MLH estimation using the nominal 0.4-m·s^{-1} threshold. Formally,

$$\sigma_{\text{MLH},k}^{\text{DWL},\pm} = \left| z_{\text{MLH},k}^{\text{DWL (th=0.4}\pm0.1)} - z_{\text{MLH},k}^{\text{DWL (th=0.4)}} \right| \qquad (10)$$

where the plus *(minus)* superscript in $\sigma_{\text{MLH},k}^{\text{DWL},\pm}$ denotes the upper *(lower)* uncertainty bound, which is computed by inserting threshold th = 0.4 + 0.1 m·s^{-1} (th = 0.4 − 0.1 m·s^{-1}) in the first term of the right-hand side of (10) above. A similar approach was previously employed by Villalonga *et al.* [54].

C. MLH Estimation From MWR Data

1) MLH Estimation Method: The parcel method is commonly used for MLH estimation using potential temperature data [3], [7]. For a given profile of physical temperature, $T(z)$, retrieved from brightness measurements, the first step is to convert it to potential temperature profile, $\theta(z)$, by using

$$\theta(z) = T(z) \left(\frac{p_0}{p(z)} \right)^{\frac{R}{C_p}} \qquad (11)$$

where p_0 is the surface atmospheric pressure, $p(z)$ is the atmospheric pressure profile, $R = 287$ J · K^{-1} · kg^{-1} is the universal gas constant, and C$_p$ = 1004 J · K^{-1} · kg^{-1} is the specific heat capacity for dry air at a constant pressure [55]. Physically, the potential temperature represents the temperature an air parcel at an altitude z if it were lowered, dry adiabatically, to the surface. In the parcel method, the MLH is defined as the lowest point in a given potential temperature profile for which $\theta(z) > \theta(0)$, where $\theta(0)$ is the surface value of the potential temperature. Small scale effects (e.g., surface properties and shielding of the sensor) can bias the estimate of surface temperature $T(0) = \theta(0)$, to which the parcel method is very sensitive [6], [56].

Changes in $\theta(z)$ with respect to height, $(d\theta/dz)$, are indicative of the stability of the atmosphere with respect to displacement of unsaturated air parcels. The atmosphere is stable when $(d\theta/dz) > 0$, neutral when $(d\theta/dz) = 0$, and unstable when $(d\theta/dz) < 0$. Under quiescent conditions in the daytime, the ML is characterized by continuous convective mixing, driven from below by buoyant thermal plumes from the relatively warm surface and, sometimes, from above, by evaporatively driven downdrafts initiated within clouds in the EZ. As a result of this continuous mixing, the interior of the ML exhibits nearly uniform temperature and moisture throughout most of its depth. Thus, $(d\theta/dz) = 0$ in the ML and negative in the surface layer (unstable), $(d\theta/dz) < 0$. At the top of the ML, an increase in temperature and reduction in moisture delineates the EZ, i.e., a transition layer between the ML and the FT. The MLH is typically computed as falling halfway between the top of the ML and the bottom of the FT,

near where the magnitudes of the temperature and/or moisture gradients are maximized.

While the parcel method was designed for use with sounding data, Stull [1] (p. 474) cautions against estimating MLH using only a single radiosounding. This is because a single radiosounding may not be representative of average conditions in a horizontally heterogeneous ML, as would be the case in a convectively active BL characterized by thermal updrafts and downdrafts. MWR offers a partial solution to this issue in that it provides a time series of potential temperature profiles. Temporal averaging can ameliorate to some extent the perturbations caused by individual updrafts and downdrafts, allowing longer term (e.g., ∼O[30 min–1 h]) trends in MLH to be discerned.

To estimate the MLH from MWR data, first, MWR potential-temperature profiles are interpolated to a uniform vertical resolution of 10 m. Second, a five-point (50 m) moving average is applied to smooth the profiles [27]. Then, the MLH-MWR is derived by using as a surface temperature reference, $\theta(0)$, from the JOYCE meteorological tower at 2 m, thus assuring reliable retrievals [6]. The tower-derived temperature, which has a raw temporal resolution of 6 min, is interpolated to the MWR temporal resolution (2.7 min).

In Fig. 3, we present an example comparison of MLH-LC-EKF [see Fig. 3(a)] with MLH-MWR [see Fig. 3(b)]. In spite of the relatively coarse spatial resolution (which decreases with height) of the MWR potential temperature profiles, it can be seen that MLH-MWR follows the overall trend of the radiosonde-derived MLH and particularly during morning (0600–1000 UTC) and evening (1600–1900 UTC) TTs MTT and ETT, respectively. The MLH-MWR captures the collapse of the convective BL during the latter period, after sunset, while the MLH-LC-EKF estimate continues to follow the elevated RL.

2) Error Estimation: The uncertainty associated with MLH-MWR has been approximated by two main error sources (see Fig. 1): 1) total uncertainty in the retrieved temperature profile $T(z)$ and consequent error propagated to the MLH calculation, which gives rise to a MLH error, Δz_T and 2) uncertainty in the estimated surface temperature, T_0 (or, equivalently, $\theta(0)$), which gives rise to a MLH error, Δz_{T_0}.

a) Assessment of the MWR-retrieved temperature-profile error in the estimated MLH, Δz_T: A study on the performance of the retrieved temperature profile [35] using a long-term dataset of representative atmospheric profiles and noise levels found uncertainty in the 0.1–0.5 K range. A synthetic brightness temperature dataset generated from over 10 000 radiosoundings (of which 5334 were used for training and 4954 were used as a validation dataset) was used to test the performance of the statistical retrieval algorithm (analogous to multiregression algorithm [57]). Altitude-dependent temperature uncertainties, $\Delta T(z)$, were generated, varying from 0.44 K on the ground to 1.60 K at 4 km. An example of the height-dependent temperature-retrieval kernels is given in Fig. 7 of [5].

In order to assess the uncertainty of MLH-MWR due to temperature-retrieval errors, Δz_T, we adopt the following approach. At each time instant, the retrieved height-dependent
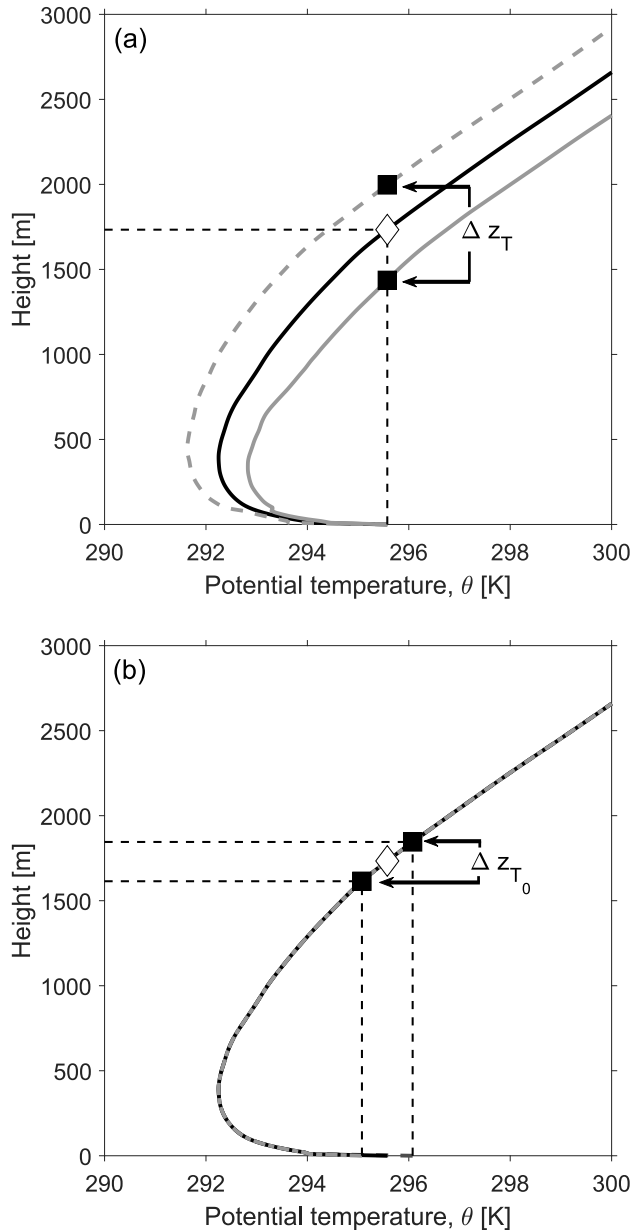
Fig. 4. Overview of MLH-MWR (parcel method) estimation errors (April 24, 2013, 1401 UTC, Jülich, Germany). (a) MLH-MWR error arising from the uncertainty inherent in the MWR retrieval of the temperature profile, Δz_T. Upper (dashed gray)- and lower (solid gray)-bound profiles are obtained by adding and subtracting the height-dependent temperature error-perturbation profile, $\Delta\theta(z)$, to the nominal potential-temperature profile, $\theta(z)$ (solid black line). The white diamond represents MLH-MWR obtained from the nominal profile, and the black squares are corresponding MLH-MWR obtained from the perturbed profiles. (b) MLH-MWR error due to the uncertainty in the measured surface temperature, Δz_{T_0}, obtained by adding and subtracting 0.5 K from the reference temperature.

temperature errors, $\Delta T(z)$, are converted into potential-temperature errors, $\Delta\theta(z)$. These are added to and subtracted from the retrieved potential temperature profile, resulting in the delineation of its "upper" and "lower" error bounds. In this approach, the uncertainty in the temperature profile acts like a bias, i.e., a consistent underestimation or overestimation throughout the profile (see also [58]). The parcel method is then applied to all three of these profiles [see Fig. 4(a)]: 1) $\theta_{MWR}(z) + \Delta\theta(z)$ or the upper error-bound profile for the

potential temperature; 2) $\theta_{MWR}(z)$ or the nominal profile; and 3) $\theta_{MWR}(z) - \Delta\theta(z)$ or the lower error-bound profile, and consequently, a MLH error bar is obtained. Fig. 4(a) shows an example error bar calculation for the temperature profiles retrieved from HATPRO MWR measurements at Jülich, Germany, at 1401 UTC on April 24, 2013. It can be observed that retrieval errors on the order of less than 2 K throughout the vertical profile introduce an uncertainty of about $\Delta z_T \approx 500$ m in the MLH estimates.

b) Assessment of surface-temperature errors on the estimated MLH, Δz_{T_0}: Following a similar perturbation approach, the uncertainty of the estimated MLH due to surface-temperature errors Δz_{T_0} is calculated by adding and subtracting the approximate uncertainty in the surface temperature (± 0.5 K) [35] to T_0. Fig. 4(b) shows three resulting MLH estimations. As a result of this perturbation in the surface temperature T_0, the uncertainty in the MLH is about 150–300 m.

Finally, the total error from error sources (a) and (b) above is computed by error superposition (see Fig. 1) as

$$\left|\Delta z_{MLH}^{MWR}\right| = \sqrt{\left|\Delta z_T\right|^2 + \left|\Delta z_{T_0}\right|^2}. \tag{12}$$

D. MLH Estimation From Radiosonde Data

The procedure to estimate the nominal MLH from RS data is the parcel method (refer to Section III-C). RS-MLH errorbars are derived in similar fashion to Section III-C2-B assuming ± 0.5 K surface temperature uncertainty. Unlike the uncertainty for temperature profiles $T(z)$ retrieved from MWR, however, the uncertainty associated with RS-measured $T(z)$ is not altitude dependent, but constant (± 0.5 K) with height. Thus, $\left|\Delta z_{MLH}^{RS}\right| = \pm$ 150–300 m.

E. 30-min Averaged MLH Retrievals and Error Assessment

In order to intercompare MLH retrievals in a meaningful statistical sense, we standardize MLH-LC-EKF, MLH-MWR, and MLH-DWL to a common temporal resolution of 30 min via maximum likelihood (MaxL) as [59]

$$MLH_X(t_h) = \frac{\sum_k z_k/\sigma_k^2}{\sum_k 1/\sigma_k^2} \tag{13}$$

where X stands for the instrument or method used ($X =$ EKF, MWR, DWL), t_h is the center time of the 30-min time window ($t_h = 0630, 0700, \dots, 2000$ UTC), z_k (formally, $z_k = z_{MLH,k}^X$) is the instantaneous MLH estimated at time $t_k \in [t_h - 15\,\text{min}, \dots, t_h + 15\,\text{min}]$, i.e., with the raw temporal resolution of the instrument/method X, and σ_k (formally, $\sigma_k = \sigma_{MLH,k}^X$) is the associated uncertainty of MLH estimate z_k. σ_k is computed via (8), (12), and (10) for the MLH-LC-EKF, MLH-MWR, and MLH-DWL, respectively.

The associated 30-min MLH uncertainty is computed as

$$\sigma_X(t_h) = \sqrt{\sigma_{X_1}^2(t_h) + \sigma_{X_2}^2(t_h)} \tag{14}$$

where σ_{X_1} is the STD of the estimated MLH by instrument or method X (a proxy of the instantaneous MLH variability)

$$\sigma_{X_1} = \text{std}(z_k) \tag{15}$$

and σ_{X_2} is the uncertainty associated with the MLH estimation by instrument or method X

$$\sigma_{X_2}(t_h) = \sqrt{\frac{1}{\sum_k 1/\sigma_k^2}}. \tag{16}$$

In Section IV, intercomparisons of 30-min MLH will be performed on pairs of instruments. Bias between instruments X and Y is computed as

$$bias^{X,Y}(t_h) = \mathrm{MLH}_X(t_h) - \mathrm{MLH}_Y(t_h) \tag{17}$$

and bias variability as

$$\sigma_{\mathrm{bias}}^{X,Y}(t_h) = \sqrt{\sigma_X(t_h)^2 + \sigma_Y(t_h)^2}. \tag{18}$$

F. Ceilometer-MWR Synergistic (SYN) Method

The MLH-LC-EKF and MLH-MWR methods feature contrasting behaviors, as exemplified in Fig. 3(a). On the one hand, MLH-MWR uncertainties span several hundred meters (blue error bars) and expand with height as a consequence of the MWR coarser spatial resolution at higher altitudes. On the other hand, MLH-LC-EKF have much smaller uncertainties (magenta error bars), on the order of tens of meters, which lie within those of MLH-MWR when the ABL is well developed (e.g., 1000–1400 UTC). However, during the ETT (1500–1800 UTC), MLH-LC-EKF detaches from the ABL, following the RL, instead.

Accordingly, we are motivated to introduce a synergistic MLH estimation method (SYN), which yields an optimal MLH estimate (MLH-SYN) that improves upon MLH-MWR and MLH-LC-EKF estimates considered in isolation. The SYN method combines the 30-min MLH retrievals and associated uncertainties of these two methods as follows: the MLH estimate provided by the SYN, $\mathrm{MLH}_{\mathrm{SYN}}$, is computed as follows:

1) The maximum likelihood between MLH-LC-EKF and MLH-MWR as

$$\mathrm{MLH}_{\mathrm{SYN}}(t_h) = \frac{\frac{\mathrm{MLH}_{\mathrm{EKF}}(t_h)}{\sigma_{\mathrm{EKF}}^2(t_h)} + \frac{\mathrm{MLH}_{\mathrm{MWR}}(t_h)}{\sigma_{\mathrm{MWR}}^2(t_h)}}{1/\sigma_{\mathrm{EKF}}^2(t_h) + 1/\sigma_{\mathrm{MWR}}^2(t_h)}$$
$$\mathrm{if}\ I_{\mathrm{EKF}}(t_h) \cap I_{\mathrm{MWR}}(t_h) \neq \emptyset \tag{19}$$

   in two situations.

   a) When their respective MLH uncertainty intervals [see (14)], $I_{\mathrm{EKF}}(t_h) = [\![\mathrm{MLH}_{\mathrm{EKF}}(t_h) - \sigma_{\mathrm{EKF}}(t_h), \mathrm{MLH}_{\mathrm{EKF}}(t_h) + \sigma_{\mathrm{EKF}}(t_h)]\!]$ and $I_{\mathrm{MWR}}(t_h) = [\![\mathrm{MLH}_{\mathrm{MWR}}(t_h) - \sigma_{\mathrm{MWR}}(t_h), \mathrm{MLH}_{\mathrm{MWR}}(t_h) + \sigma_{\mathrm{MWR}}(t_h)]\!]$ overlap at least partially [i.e., (19)].

   b) When t_h falls in a strongly convective period, $I = [1000–1400]$ UTC. I corresponds to mid-afternoon at the JOYCE site when, assuming quiescent atmospheric conditions, the CBL reaches its maximum depth and maturity. In a more generalized formulation, I would be location-dependent.

The associated uncertainty for the synergistic MaxL estimate of (19) above is given by

$$\sigma_{\mathrm{SYN}}(t_h) = \sqrt{\frac{1}{1/\sigma_{\mathrm{EKF}}^2(t_h) + 1/\sigma_{\mathrm{MWR}}^2(t_h)}}. \tag{20}$$

2) The MLH-MWR estimates elsewhere (i.e., out of statements (i.a) and (i.b) above). Formally,

$$\begin{cases} \mathrm{MLH}_{\mathrm{SYN}}(t_h) = \mathrm{MLH}_{\mathrm{MWR}}(t_h) \\ \sigma_{\mathrm{SYN}}(t_h) = \sigma_{\mathrm{MWR}}(t_h). \end{cases} \tag{21}$$

   In this latter case, the uncertainty of the MLH-SYN is equal to that of MLH-MWR [see (14)].

Equation (19) is essentially the MaxL definition given by (13) but applied to each pair of MLH estimates, EKF, and MWR at each 30-min time step, t_h. The SYN method is discussed next in Section IV-A.

In case (i), this formulation balances MLH-LC-EKF and MLH-MWR estimates by attributing higher weight to the estimates with lower uncertainty. Typically, MLH-LC-EKF is favored during the mid-afternoon peak in CBL growth. Case (ii) typifies MLH development or decay during MTT and ETT, respectively. During these periods, MLH-LC-EKF and MLH-MWR tend to diverge, and the SYN method retains MLH-MWR as the most reliable estimate. This constraint ensures that the SYN method avoids MLH-LC-EKF tracking the RL (i.e., layer-attribution error).

IV. DISCUSSION

30-min MLH-SYN estimates are compared to MLH-LC-EKF, MLH-MWR, and MLH-DWL (see Section III) considered in isolation with reference to MLH-RS. The statistical analysis is limited to the 0600–2030 UTC time interval, which delineates the CBL diurnal cycle, including MTT and ETT over the JOYCE site. Section IV-A discusses the SYN in the context of one "textbook" clear-day example. Section IV-B gives an overview of the campaign dataset. Section IV-C evaluates performance statistics of the different MLH retrieval methods for the whole campaign.

A. SYN Example

Case day 20 April 2013 [see Fig. 3(a)] is used to exemplify the SYN retrieval in Fig. 5(a). MLH estimates derived from the different methods are plotted with 30-min resolution (13). This day was characterized by a cloud-capped mixing layer from 0700 to 1100 UTC and by clear sky otherwise. For visual reference in the plots next, MTT is defined as [0600–1000) UTC, ETT as [1400–2030) UTC, and peak CBL growth time as [1000–1400) UTC. Solar noon at JOYCE is 1130 UTC.

From 0600 to 0800 UTC, MLH-LC-EKF, MLH-MWR and MLH-DWL track closely with one another but fall below MLH-RS [see Fig. 5(a)]. The MLH-LC-EKF agreed well with MLH-MWR despite the presence of aerosols in the 500–1000-m layer. In contrast, MLH-DWL fell slightly below MLH-MWR because of the relatively weak turbulence in the early morning and the the use of a constant VVSTD threshold (see Section III-B). MLH estimates from all methods coincided from 0800 to 1500 UTC. In other words, during most of this interval (case (i.a) in Section III-F), the MLH-LC-EKF and MLH-MWR errorbars [computed as the $\pm 3\sigma$ value from (14)] partially or totally overlapped, and hence,
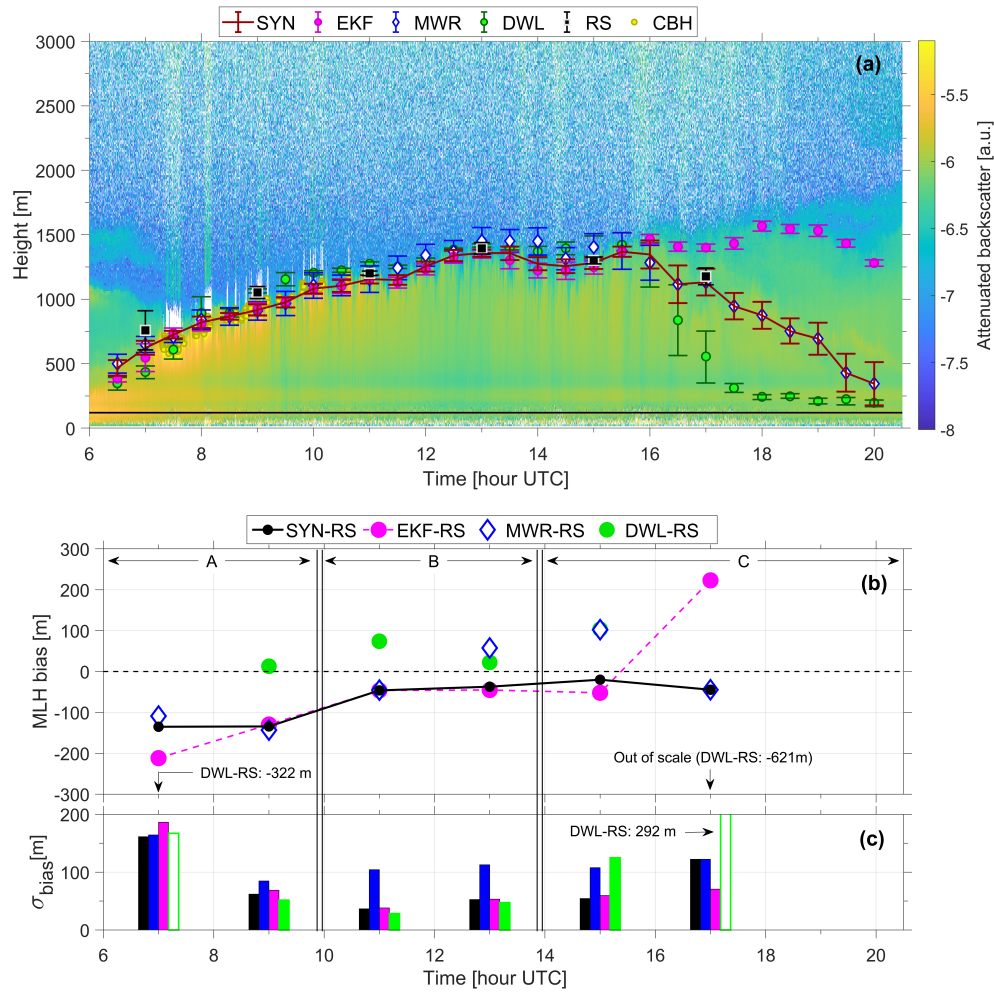
Fig. 5. Performance of the SYN algorithm and MLH-LC-EKF, MLH-MWR, and MLH-DWL methods in isolation with reference to MLH-RS estimates as function of hour of day (case 20 April 2013, Fig. 3). (a) 30-min MLH estimates (13). (b) MLH bias (17). (c) MLH bias variability (18). Labels A, B, and C indicate typical MTT, peak convective, and ETT intervals, respectively (see Section IV-A).

the MLH-SYN) was the MaxL estimate between the MLH-LC-EKF and MLH-MWR retrievals in isolation (19) with an associated uncertainty given by (20).

During the strongly convective interval, 1000 to 1400 UTC (case (i.b) in Section III-F), the ML-to-FT gradient was sharply defined, and reliability of MLH-LC-EKF increased, with values closer to MLH-RS. In this interval, the ML was free from layer attribution errors, and the MLH-SYN was constrained to the MaxL value between MLH-LC-EKF and MLH-MWR, irrespective of whether their individual error bars overlapped (e.g., at 1400 UTC). The latter shows the case of thermal updrafts causing MLH-MWR and MLH-DWL to jump slightly above the smoother MLH-LC-EKF time series. As a result of the smaller MLH-LC-EKF error bars during this interval, the MLH-SYN followed MLH-LC-EKF and inherited its smaller uncertainty (20).

After 1500 UTC (i.e., the start of the ETT), each MLH estimate started to develop a distinct behavior: MLH-DWL fell quickly as thermal turbulence decayed, whereas MLH-MWR decreased smoothly, thus coinciding with the radiosonde at 1700 UTC. In contrast, MLH-LC-EKF kept on tracking the elevated aerosol layer, which became the RL. In this situation,

MLH-SYN followed MLH-MWR (case (ii) in Section III-F), with MLH-SYN error bars overlapping MLH-MWR error bars [plotted in dark red and blue, respectively, in Fig. 5(a)], therefore avoiding layer-attribution errors typical of MLH-LC-EKF in the ETT.

Bias performance of the different MLH estimation methods with reference to MLH-RS is shown in Fig. 5(b). MLH-SYN and MLH-MWR (labeled SYN-RS and MWR-RS, respectively) yielded bias (17) of less than ± 150 m during the whole period (0600–1400 UTC). In addition, MLH-SYN bias variability (18) was always lower than that of MLH-MWR (see Fig. 5(c), SYN-RS and MWR-RS bars), which increases our confidence in the SYN algorithm. In the highly convective time interval B, it is evident that the MLH-LC-EKF bias variability is much lower than that of MLH-MWR (see Fig. 5(c), EKF-RS and MWR-RS bars). MLH-DWL bias in the 0900–1500 UTC interval (corresponding to the well-developed ML) was $\pm \sim 100$ m, comparable to MLH-SYN bias. However, outside of this interval (e.g., at 0700 and 1700 UTC, empty green circles) MLH-DWL bias dramatically increased to 300 and 600 m, respectively. As mentioned in Section III-B, this is a consequence of using a constant VVSTD threshold.

B. Dataset Overview

Having examined a single case day in detail, we now expand our analysis to consider the entire dataset from the 31-day HOPE campaign (April 1 to June 6, 2013), which included 80 radiosondes.

Twenty-one days were selected from this set with a total of 55 radiosondes available. Selected days were either clear-sky days (cloud cover below 3 km lower than 10%, eight days) or cloudy days (cloud cover below 3 km not greater than 70%, 13 days): clear-sky days included days with single [see Fig. 5(a)] or multiple aerosol layers [see Fig. 6(a)] in the TTs. Cloudy days were characterized by a cloud-capped BL [see Fig. 6(b)], sometimes with additional midlevel clouds well above the BL [see Fig. 6(c)]. Eight of the selected days included light drizzle events (< 0.5 mm/h, < 30 min/event, accumulated rain (0600–2000 UTC) < 0.1 mm), which usually occurred during MTT or ETT. Excluded days (ten) were days with cloud cover below 3 km greater than 70% (seven days) and rainy days (rain intensity $>= 0.5$ mm/h, two days).

During the period of peak CBL growth (1000–1430 UTC), CBHs are usually at the same height as the MLH [see Fig. 6(b)], as is common in the spring and summer time [27]. MLH-RS using the parcel method overestimated the MLH at 11, 13, and 15 UTC by some 300 m, which motivated us to compare MLH-RS with the MLH retrieved using another thermodynamically based alternative, the bulk Richardson number (BRN) method [27]. Like the parcel method, the BRN method is also based on the temperature profile but less sensitive to perturbations in the surface temperature, T_0. For consistency when computing statistics for the whole campaign, we retain MLH-RS using the parcel method.

Virga (precipitation streamers attached to the base of the clouds, e.g., in Fig. 6(c) from 1730–2000 UTC) was also problematic for MLH-LC-EKF, which tended to track the sharp gradient at the cloud tops from 1800 UTC onward. Because cloud cover strongly changes the incoming solar radiation and, consequently, ML growth, cloudy days are particularly challenging for MLH-DWL, which uses VVSTD as a proxy of the turbulent mixing. Qualitatively, the SYN algorithm delineated fairly well the typical ML diurnal cycle [see Fig. 6(a)–(c)].

C. Performance Statistics

In this subsection, statistical measures of central tendency and variability for the 21-day sample considered are used to demonstrate the superiority of MLH-SYN over MLH-MWR and MLH-LC-EKF estimates considered in isolation. Definitions for the statistical indicators are given in Appendix A.

During the course of this research, it was found that MLH-DWL performance statistics for the whole campaign are inferior to those of the other MLH estimation methods, mainly because MLH-DWL is hampered by the use of a fixed VVSTD threshold. In particular, during MTT and ETT, intermittent turbulence tends to cause MLH-DWL instability if the threshold is not adjusted. Dynamic adjustment of the VVSTD threshold in MLH-DWL falls beyond the scope of
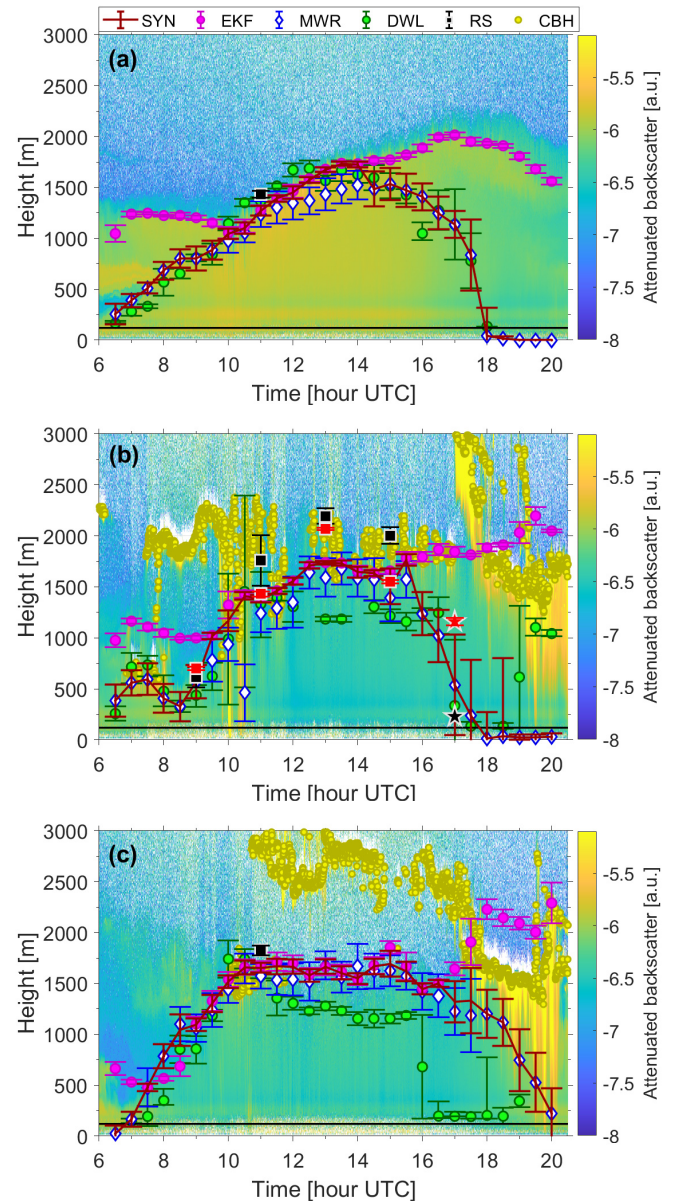
Fig. 6. As in Fig. 5(a), but representing the three typical atmospheric modes observed during the HOPE campaign: (a) clear-sky day (April 22, 2013) showing multiple aerosol layers from 0600 to 1000 UTC; (b) partially cloud-capped BL day (April 13, 2013); and (c) midlevel cloud day (May 16, 2013) with virga from 1730 to 2000 UTC. In (b), red squares are MLH estimates made using BRN derived from RS $\theta(z)$ profiles. Black and red stars at 1700 UTC indicate the stable BL height estimates retrieved by the gradient method and BRN, respectively.

the present work. MLH-DWL performance characteristics will nonetheless be reported in this study in order to motivate future research in this area.

1) MLH Estimates by the Different Methods: MLH estimates averaged over the selected 21 days as a function of hour of day (local time) are shown in Fig. 7(a). While both MLH-MWR and MLH-EKF methods were based on 21 samples [one for each hour, each day; see Fig. 7(b)], MLH-DWL furnished fewer samples during MTT (0600–0800 UTC) and ETT (1600–2030 UTC), open green circles). In these time intervals, MLH-DWL was often <120 m, and such
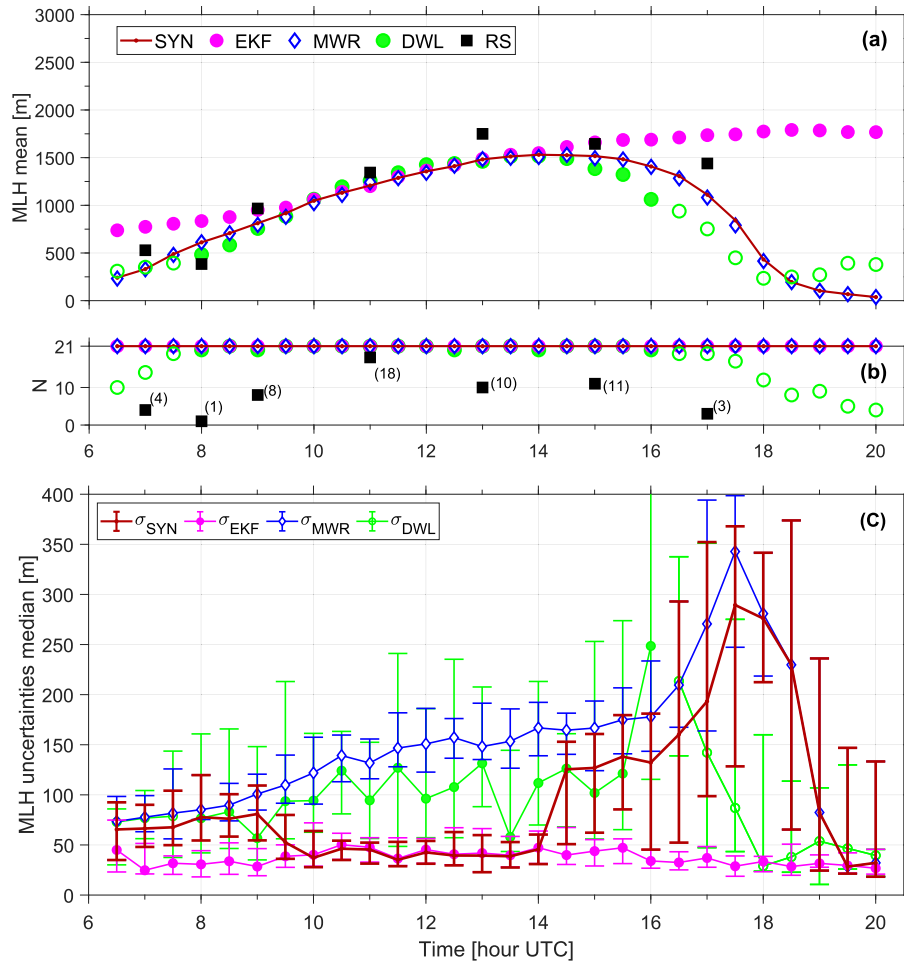
Fig. 7. Means and uncertainties of 30-min MLH estimates over the selected 21 clear-sky days as a function of hour of day in UTC (LT=UTC+1h). (a) (Top panel) means (A.1) of MLH-SYN (red solid trace), MLH-LC-EKF (magenta dots), MLH-MWR (white diamonds), MLH-DWL (green dots), and MLH-RS (black squares). (b) Number of case days (out of 21 total days) used to compute mean values. (c) Median values (markers) and interquartile ranges (bars) of the 30-min MLH uncertainties (14).

estimates were rejected as outliers by the reasoning discussed in Section III-B.

The best agreement among all MLH estimation methods occurred from 1000 to 1400 UTC. As previously mentioned, this is the interval in which, under quiescent conditions, intensive, thermally driven convection deepens the CBL, and, consequently, MLH reaches its highest altitudes of the daily cycle [1]. The MLH-LC-EKF attribution-layer error clearly evidenced during MTTs and ETTs, during which the SYN algorithm successfully took over. From 0600 to 0900 UTC, the MLH-LC-EKF exceeded MLH from other estimators, revealing that MLH-LC-EKF retrievals were frequently affected by the persistent aerosol layers from the previous night. During early the morning, the MLH-SYN followed MLH-MWR. Both rose in concert with MLH-RS 0700 and at 0900 UTC. MLH-SYN, MLH-MWR, and MLH-DWL rose together until 1400 UTC. As exemplified by previously discussed case of April 20, 2013 (see Fig. 5), the disagreement among all MLH estimation methods grew sharply from 1500 UTC onward (i.e., the start of the ETT) when the turbulence decayed, the CBL separated from the RL, and the stable BL began to form in response to the reversal of surface

radiative flux. MLH-LC-EKF tracked this RL. While MLH-DWL properly tracked the turbulence decay, it exhibited worse agreement than MLH-MWR with MLH-RS at 1700 UTC [see Fig. 7(a)].

30-min MLH estimation uncertainty (14), as a function of hour of day, is shown in Fig. 7(c) by computing medians and interquartile ranges (25-to-75-th percentiles) for the total sample of 21 days. MLH-LC-EKF exhibited much lower medians (by ≈40 m) and spreads than MLH-MWR in all hours of the strongly convective period (e.g., ≈140 m, 1000–1400 UTC). This result further favors the SYN algorithm during this interval.

2) Performance of the SYN Method and of MWR and EKF Methods in Isolation With Reference to RS Retrievals:

a) MLH bias versus RS: MLH mean bias (MB) [see Fig. 8(a) and (A.3)] is computed as the difference between the 21-day means of MLH-SYN, MLH-MWR, MLH-DWL, and MLH-RS estimates in a 30-min time window centered at the RS launch time.

MLH-SYN and MLH-MWR yielded mean biases less than ±150 m overall (SYN-RS and MWR-RS labels in Fig. 8(a), respectively), and −150 m during the convective
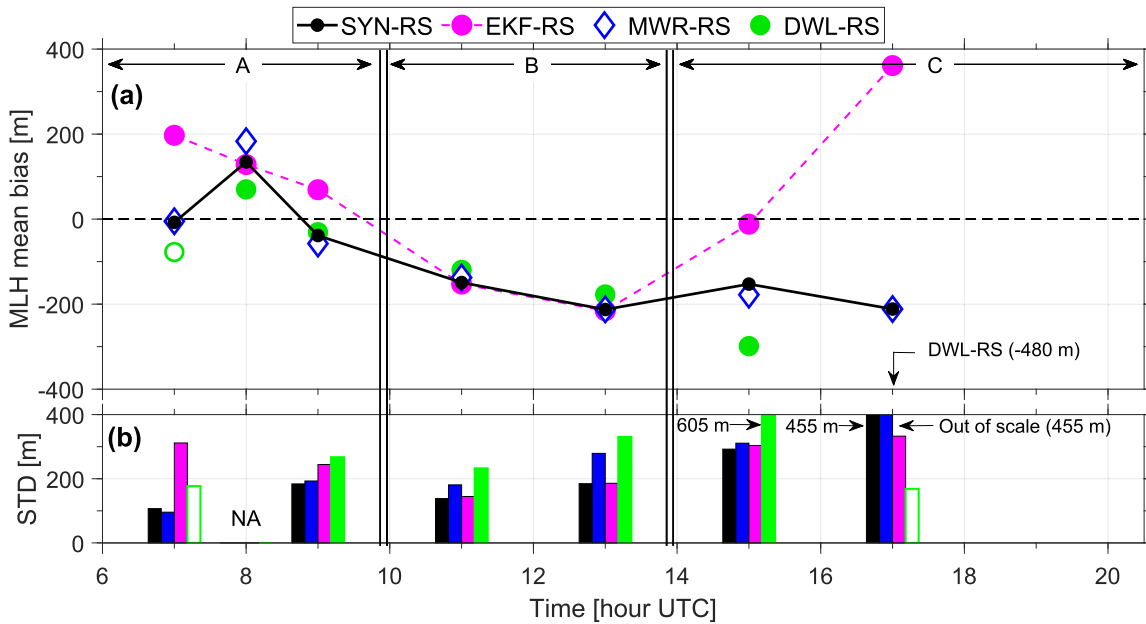
Fig. 8. Biases relative to MLH-RS of the 30-min MLH estimations over the selected 21 clear-sky days as a function of hour of day in UTC. (a) Mean biases. Label "X-RS" (X=SYN, EKF, MWR, DWL) stands for the MB $\mu_{\text{bias}}^{X,RS}(t_h)$ (A.3) between an instrument/method combination X and MLH-RS. (b) Mean biases STD $\sigma_{\text{bias}}^{X,RS}(t_h)$ (A.4).

interval (B; 1000–1400 UTC). The latter is consistent with the findings of [18] (see Fig. 4(a) therein) who estimated bias of ≈200 m for MLH-LC-EKF. As expected, MLH-LC-EKF [EKF-RS label in Fig. 8(a)] performed poorly outside the 1000–1400 UTC convective interval (B), during the MTT and ETT. Its V-shaped MB curve reaches +200 and +400 m at 0700 and 1700 UTC, respectively.

b) MLH bias-to-RS variability: MLH bias-to-RS variability [see Fig. 8(b)] is computed as the STD given by (A.4). Because all the MLH estimates are subject to the same atmospheric, day-to-day variability, comparative differences in bias STD among them are attributable to their individual performance. Therefore, each hourly set of vertical bars ranks the different MLH estimation methods by bias performance with reference to RS. Thus, in the convective interval (1000–1400 UTC), MLH-LC-EKF and MLH-SYN had the lowest bias STD (EKF-RS and SYN-RS labels, respectively). In contrast, during TTs, MLH-MWR and MLH-SYN exhibited the lowest bias STD. In summary, the the SYN algorithm performed best over the whole daily interval because it inherited the superior performance characteristics of its constituent methods. MLH-LC-EKF performance in TTs was—as expected—worst [see Fig. 8(a)]. MLH-DWL only gave usable estimates between 900 and 1500 UTC, and even then, its performance (green bars) was always worse than that of the MWR (blue bars). Outside of this interval, there were retrieval issues (empty green dots) related either to the selection of a fixed VVSTD threshold or MLHs below the instrument minimum measurable height of 120 m.

c) Correlation and regression analysis: Fig. 9 compares the different MLH retrievals to MLH-RS [e.g., $X = \text{MLH}_{\text{RS}}$ and $Y = \text{MLH}_{\text{MWR}}$ in panel (a)]. Two time intervals were investigated: *(i) one capturing the full*

daytime diurnal cycle [0600–2030) UTC, which included 55 radiosondes and *(ii) the shorter, strongly convective period in the local afternoon* [0930–1430) UTC, which included 28 radiosondes. MLH MB values in each of these two time intervals were comparable for both SYN and MWR methods. In addition, the MB obtained in time intervals *(i)* and *(ii)* (red and blue text labels, respectively) for each method approximately coincided with the average of the hourly biases plotted in Fig. 8(a) in these intervals. The root-mean-square error (RMSE) was slightly lower for the SYN method ($\text{RMSE}_{\text{SYN}}^{(i)} = 247$ m and $\text{RMSE}_{\text{MWR}}^{(i)} = 278$ m; see labels) and relatively high for the DWL $\text{RMSE}_{\text{SYN}}^{(i)} = 393$ m. The latter value is in accordance with the RMSE of 359 m (0800–1600 UTC) reported by Schween *et al.* [27]. All RMSE indicators improved in convective time interval 2) because of the lower variability of the MLH.

The significance of the indicators above warrant some comments. Gross outliers were particularly abundant during TTs. Gross outliers are defined as biased estimates (MLH_X-MLH_{RS}, $X = \text{SYN, EKF, MWR, DWL}$) above $\pm 1\sigma$ of the mean of the associated MLH bias histogram computed hourly. To further improve the significance of results, gross outliers were removed prior to evaluating correlation statistics via a similar procedure as that described in [18] and [60]. When Fig. 9 was regenerated after gross outliers were removed (not shown), the linear regression lines ("RL" subscript in Fig. 9) became virtually coincident with the 1:1 line, indicating virtually no bias. Furthermore, MLH-SYN remained superior to MLH-MWR and MLH-DWL. In the diurnal time interval *(i)* above, the SYN exhibited $\rho_{\text{SYN},1\sigma}^{(i)} = 0.98$ and $\text{RMSE}_{\text{SYN},1\sigma}^{(i)} = 76$ m, followed by the MWR, $\rho_{\text{MWR},1\sigma}^{(i)} = 0.96$ and $\text{RMSE}_{\text{MWR},1\sigma}^{(i)} = 103$ m, and the DWL, $\rho_{\text{DWL},1\sigma}^{(i)} = 0.95$ and $\text{RMSE}_{\text{DWL},1\sigma}^{(i)} = 157$ m. Over the convective time interval *(ii)*, the SYN
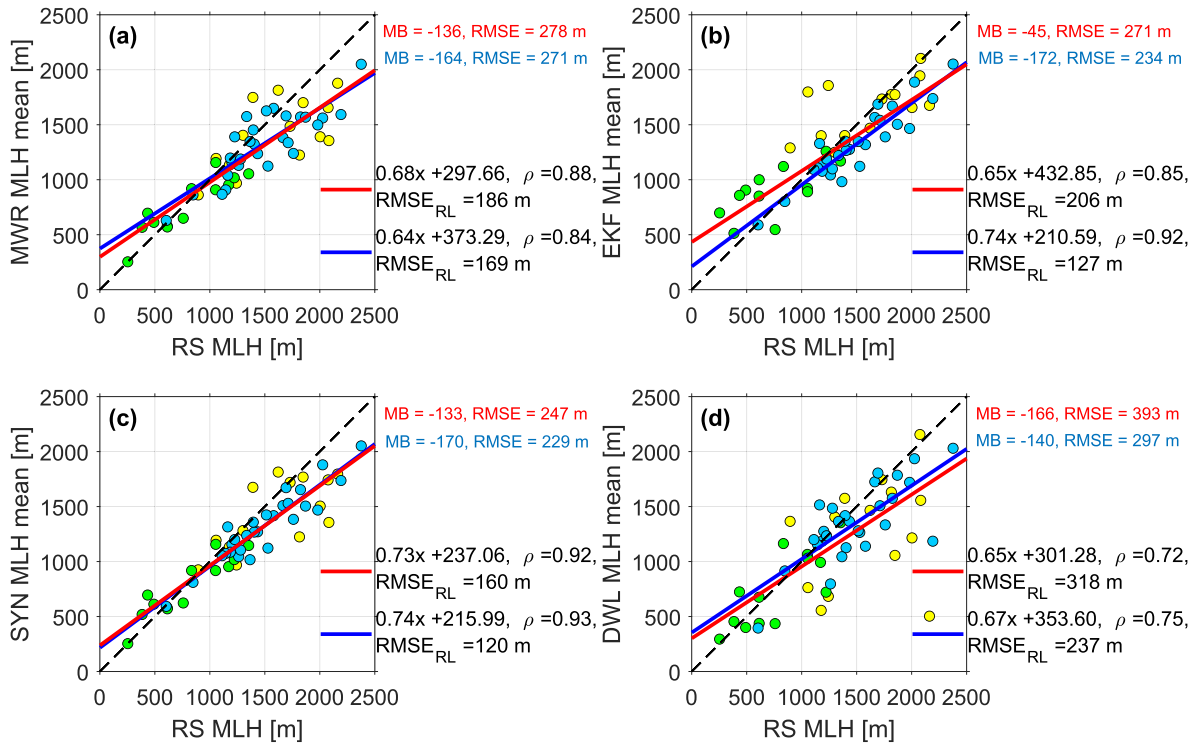
Fig. 9. Scatterplot comparison of 21 clear-sky day, 30-min (a) MLH-MWR, (b) MLH-LC-EKF, (c) MLH-SYN, and (d) MLH-DWL with MLH-RS. Green, blue, and yellow dots depict MLH estimates in the [0600–0930), [0930–1430), and [1430–2030) UTC time intervals, respectively. Red and blue lines are regression lines over diurnal [0600–2030) UTC and convective [0930–1430) UTC MLH estimates, respectively. RMSE$_{RL}$ denotes regression-line root-mean-square error. For reference in all panels, the 1:1 line is drawn as a black dashed line. MB and RMSE are annotated in colors corresponding to their respective time intervals.

achieved $\rho_{SYN,1\sigma}^{(ii)} = 0.99$ and RMSE$_{SYN,1\sigma}^{(ii)} = 41$m (compared to $\rho_{MWR,1\sigma}^{(ii)} = 0.94$ and RMSE$_{MWR,1\sigma}^{(ii)} = 86$m prior to gross outlier removal).

V. CONCLUSION

A synergistic MLH retrieval algorithm combining MWR and ceilometer-based estimates was presented along with performance statistics covering 21 days of the HOPE campaign. The SYN method used a maximum-likelihood algorithm (see Section III-F) that combined MLH-LC-EKF and related error uncertainties in the strongly convective BL time interval (local afternoon, which, at JOYCE, is 1000–1400 UTC) with MLH-MWR and associated uncertainties outside of this interval. MLH-LC-EKF were derived from the ML-to-FT gradient in the attenuated backscatter profile by using a Kalman filter, yielding time-adaptive MLH estimates with a temporal resolution equal to that of the LC. MLH-MWR was estimated by the parcel method applied to MWR-derived temperature profiles.

The motivation for creating MLH-SYN, which combined MLH estimates by different methods, was the inherent weaknesses each method exhibited in isolation. Specifically, MLH-LC-EKF tends to track aerosol gradients, which led the filter to follow RLs during MTT and ETT. The latter was the most common layer-attribution error. In experiments, the EKF was able to detect gradients as low as 1.5–1 times the mean FT level [see Fig. 2(a)]. Assuming no attribution errors, the MLH uncertainty was given by the *a posteriori* error of the filter

(see Section III-A2). We, therefore, formulated MLH-SYN to equal MLH-LC-EKF in the strongly convective afternoon interval (1000–1400 UTC). Outside this interval, MLH-MWR proved more reliable with an uncertainty given by the inherent error in the MWR-retrieved temperature profile and parcel-method surface-temperature error (see Section III-C). MLH-DWL was excluded from the formulation of MLH-SYN; intermittent turbulence, particularly during the ETT, along with the assumption of a fixed VVSTD threshold, was the major issue.

The variability in MLH estimation uncertainty matched that of its component algorithms (MLH-MWR and MLH-LC-EKF) as a function of time of day [see Fig. 7(b)]. Specifically, during the strongly convective interval (1000–1400 UTC), the MLH-SYN exhibited ≈40 m (median) compared to ≈140 m by MLH-MWR, which indicates that SYN inherited the steady tracking performance of the MLH-LC-EKF. Outside this interval, the variability of MLH-SYN approached that of MLH-MWR.

Comparative performance of the different MLH estimation methods with reference to MLH-RS was also addressed. The statistical analysis over the 21-day sample showed that MLH MB was inflated by gross outliers associated with TTs and day-to-day atmospheric variability. In addition, the parcel method (used in both MLH-MWR and MLH-RS) was particularly sensitive to the accuracy of surface temperature T_0. Nonrepresentativeness of T_0 on specific days involving complex micrometeorological effects was a challenging

difficulty. Nonetheless, with reference to radiosoundings (with and without outlier removal from the data collection), the SYN algorithm outperformed all other MLH estimation methods in isolation. In the $diurnal^{(i)}[\![convective^{(ii)}]\!]$ time interval, MLH-SYN achieved a correlation coefficient $\rho_{\mathrm{SYN},1\sigma}^{(i)(ii)} \geq 0.98$ and RMSE, $\mathrm{RMSE}_{\mathrm{SYN},1\sigma}^{(i)} = 76$ m ($\mathrm{RMSE}_{\mathrm{SYN},1\sigma}^{(ii)} = 41$ m). These results compare favorably to MLH-MWR alone: $\rho_{\mathrm{MWR},1\sigma}^{(i)(ii)} \geq 0.94$ and $\mathrm{RMSE}_{\mathrm{MWR},1\sigma}^{(i)} = 103$ m ($\mathrm{RMSE}_{\mathrm{MWR},1\sigma}^{(ii)} = 86$ m).

To sum up, although SYN used the simplistic assumption of a fixed strongly convective time interval (1000–1400 UTC), the time-adaptive combination of two largely independent methods for MLH tracking, one based on aerosol gradient-based observations (MLH-LC-EKF) and the other temperature-based (MLH-MWR), has shown superior MLH tracking skill. Further research is planned to extend this methodology over the whole diurnal cycle, as well as to explore further synergy with DWL sensors. Besides, a comparison of all the sources of uncertainty in terms of how they balance and propagate would be an interesting study for the remote sensing community.

APPENDIX A
MEASURES OF CENTRAL TENDENCY AND VARIABILITY

The mean of the 30-min MLH for the instrument/method combination, X, denoted $\mu_{\mathrm{MLH},X}(t_h)$, is computed at time t_h as

$$\mu_{\mathrm{MLH},X}(t_h) = \frac{1}{N}\sum_{i=1}^{N}\mathrm{MLH}_X(t_h, d_i) \qquad (A.1)$$

where $N = 21$ is the total number of selected days (statistical sample) and d_i denotes the ith day, $i = 1, \ldots, N$. The variability of the estimated MLH in (A.1) above is computed as the STD over the sample population

$$\sigma_{\mathrm{MLH},X}(t_h) = \sqrt{\frac{1}{N}\sum_{i=1}^{N}\left(\mathrm{MLH}_X(t_h, d_i) - \mu_{\mathrm{MLH},X}(t_h)\right)^2}. \quad (A.2)$$

The mean of the MLH bias (17) between MLH estimates from two different instruments/datasets denoted X and Y is computed at each time t_h as

$$\mu_{\mathrm{bias}}^{X,Y}(t_h) = \frac{1}{N}\sum_{i=1}^{N}\mathrm{bias}^{X,Y}(t_h, d_i). \qquad (A.3)$$

The variability of the MLH bias given by (A.3) above is computed as the STD

$$\sigma_{\mathrm{bias}}^{X,Y}(t_h) = \sqrt{\frac{1}{N}\sum_{i=1}^{N}\left(\mathrm{bias}^{X,Y}(t_h, d_i) - \mu_{\mathrm{bias}}^{X,Y}(t_h)\right)^2}. \quad (A.4)$$

ACKNOWLEDGMENT

CommSensLab -UPC is a María-de-Maeztu Excellence Unit (MDM-2016-0600) funded by the Agencia Estatal de Investigación, Spain. Data were provided by Jülich Observatory for Cloud Evolution (JOYCE-CF), a core facility (CF) funded by Deutsche Forschungsgemeinschaft via Grant DFG LO 901/7-1. Dr. J. H. Schween and Prof. S. Crewell are thanked for the stay of U. Saeed at the Institute for Geophysics and Meteorology, University of Cologne, and data provision. Three unknown reviewers are also thanked for their insightful comments to this article.

REFERENCES

[1] R. B. Stull, *An Introduction to Boundary Layer Meteorology*. Amsterdam, The Netherlands: Springer, 1988.

[2] S. Emeis, *Surface-based Remote Sensing of the Atmospheric Boundary Layer*. Dordrecht, The Netherlands: Springer, 2010.

[3] P. Seibert, F. Beyrich, S.-E. Gryning, S. Joffre, A. Rasmussen, and P. Tercier, "Review and intercomparison of operational methods for the determination of the mixing height," *Atmos. Environ.*, vol. 34, no. 7, pp. 1001–1027, 2000.

[4] G. Xu et al., "Comparison of atmospheric profiles between microwave radiometer retrievals and radiosonde soundings," *J. Geophys. Res., Atmos.*, vol. 120, no. 19, pp. 10313–10323, Oct. 2015.

[5] U. Löhnert and O. Maier, "Operational profiling of temperature using ground-based microwave radiometry at payerne: Prospects and challenges," *Atmos. Meas. Techn.*, vol. 5, no. 5, pp. 1121–1134, May 2012.

[6] M. Collaud Coen, C. Praz, A. Haefele, D. Ruffieux, P. Kaufmann, and B. Calpini, "Determination and climatology of the planetary boundary layer height above the Swiss plateau by *in situ* and remote sensing measurements as well as by the COSMO-2 model," *Atmos. Chem. Phys.*, vol. 14, no. 23, pp. 13205–13221, Dec. 2014.

[7] G. C. Holzworth, "Estimates of mean maximum mixing depths in the contiguous United States," *Monthly Weather Rev.*, vol. 92, no. 5, pp. 235–242, 1964.

[8] G. de Arruda Moreira et al., "Study of the planetary boundary layer by microwave radiometer, elastic lidar and Doppler lidar estimations in Southern Iberian Peninsula," *Atmos. Res.*, vol. 213, pp. 185–195, Nov. 2018.

[9] L. Belegante, D. Nicolae, A. Nemuc, C. Talianu, and C. Derognat, "Retrieval of the boundary layer height from active and passive remote sensors. Comparison with a NWP model," *Acta Geophys.*, vol. 62, no. 2, pp. 276–289, Apr. 2014.

[10] D. Cimini, F. D. Angelis, J.-C. Dupont, S. Pal, and M. Haeffelin, "Mixing layer height retrievals by multichannel microwave radiometer observations," *Atmos. Meas. Techn.*, vol. 6, no. 11, pp. 4971–4998, 2013.

[11] D. Lange, J. Tiana-Alsina, U. Saeed, S. Tomás, and F. Rocadenbosch, "Atmospheric boundary layer height monitoring using a Kalman filter and backscatter lidar returns," *IEEE Trans. Geosci. Remote Sens.*, vol. 52, no. 8, pp. 4717–4728, Aug. 2014.

[12] R. E. Kalman, "A new approach to linear filtering and prediction problems," *J. Basic Eng.*, vol. 82, no.1, pp. 35–45, May 1960, doi: 10.1115/1.3662552.

[13] S. H. Melfi, J. D. Spinhirne, S.-H. Chou, and S. P. Palm, "Lidar observations of vertically organized convection in the planetary boundary layer over the ocean," *J. Climate Appl. Meteorol.*, vol. 24, no. 8, pp. 806–821, Aug. 1985.

[14] R. M. Endlich, F. L. Ludwig, and E. E. Uthe, "An automatic method for determining the mixing depth from lidar observations," *Atmos. Environ.*, vol. 13, no. 7, pp. 1051–1056, Jan. 1979.

[15] C. Senff, J. Bösenberg, G. Peters, and T. S. Chaberl, "Remote sensing of turbulent ozone fluxes and the ozone budget in the convective boundary layer with DIAL and radar-RASS: A case study," *Contrib. Atmos. Phys.*, vol. 61, no. 9, pp. 161–176, 1996.

[16] L. Menut, C. Flamant, J. Pelon, and P. H. Flamant, "Urban boundary-layer height determination from lidar measurements over the Paris area," *Appl. Opt.*, vol. 38, no. 6, pp. 945–954, 1999.

[17] W. P. Hooper and E. W. Eloranta, "Lidar measurements of wind in the planetary boundary layer: The method, accuracy and results from joint measurements with radiosonde and Kytoon," *J. Appl. Meteorol. Climatol.*, vol. 25, no. 7, pp. 100–990, 1986.

[18] R. F. Banks, J. Tiana-Alsina, F. Rocadenbosch, and J. M. Baldasano, "Performance evaluation of the boundary-layer height from lidar and the weather research and forecasting model at an urban coastal site in the north-east Iberian peninsula," *Boundary-Layer Meteorol.*, vol. 157, no. 2, pp. 265–292, Nov. 2015.

[19] D. Lange, F. Rocadenbosch, J. Tiana-Alsina, and S. Frasier, "Atmospheric boundary layer height estimation using a Kalman filter and a frequency-modulated continuous-wave radar," *IEEE Trans. Geosci. Remote Sens.*, vol. 53, no. 6, pp. 3338–3349, Jun. 2015.

[20] R. L. Tanamachi, S. J. Frasier, J. Waldinger, A. LaFleur, D. D. Turner, and F. Rocadenbosch, "Progress toward characterization of the atmospheric boundary layer over northern Alabama using observations by a vertically pointing, S-band profiling radar during VORTEX-southeast," *J. Atmos. Ocean. Technol.*, vol. 36, no. 11, pp. 2221–2246, Nov. 2019.

[21] M. Barrera-Verdejo, S. Crewell, U. Löhnert, E. Orlandi, and P. D. Girolamo, "Ground-based lidar and microwave radiometry synergy for high vertical resolution absolute humidity profiling," *Atmos. Meas. Techn.*, vol. 9, no. 8, pp. 4013–4028, 2016.

[22] M. A. LeMone *et al.*, "100 years of progress in boundary layer meteorology," *Meteorol. Monographs*, vol. 59, p. 9, Jan. 2018.

[23] A. Macke *et al.*, "The HD(CP)^2 observational prototype experiment (HOPE)–An overview," *Atmos. Chem. Phys.*, vol. 17, no. 7, pp. 4887–4914, 2017.

[24] R. M. Measures, *Laser Remote Sensing: Fundamentals and Applications* (Laser-Remote Sensor Equations). Malabar, FL USA: Wiley, 1992, ch. 7, pp. 237–280.

[25] U. Löhnert *et al.*, "JOYCE: Jülich observatory for cloud evolution," *Bull. Amer. Meteorol. Soc.*, vol. 96, no. 7, pp. 1157–1174, 2015.

[26] T. Rose, S. Crewell, U. Löhnert, and C. Simmer, "A network suitable microwave radiometer for operational monitoring of the cloudy atmosphere," *Atmos. Res.*, vol. 75, no. 3, pp. 183–200, May 2005.

[27] J. H. Schween, A. Hirsikko, U. Löhnert, and S. Crewell, "Mixing-layer height retrieval with ceilometer and Doppler lidar: From case studies to long-term assessment," *Atmos. Meas. Techn.*, vol. 7, no. 11, pp. 3685–3704, Nov. 2014.

[28] N. Eresmaa, A. Karppinen, S. M. Joffre, J. Räsänen, and H. Talvitie, "Mixing height determination by ceilometer," *Atmos. Chem. Phys.*, vol. 6, no. 6, pp. 1485–1493, May 2006.

[29] C. Münkel, N. Eresmaa, J. Räsänen, and A. Karppinen, "Retrieval of mixing height and dust concentration with lidar ceilometer," *Boundary-Layer Meteorol.*, vol. 124, no. 1, pp. 117–128, Jun. 2007.

[30] E. J. O'Connor *et al.*, "A method for estimating the turbulent kinetic energy dissipation rate from a vertically pointing Doppler lidar, and independent evaluation from balloon-borne *in situ* measurements," *J. Atmos. Ocean. Technol.*, vol. 27, no. 10, pp. 1652–1664, Oct. 2010.

[31] S. A. Cohn and W. M. Angevine, "Boundary layer height and entrainment zone thickness measured by lidars and wind-profiling radars," *J. Appl. Meteorol.*, vol. 39, no. 8, pp. 1233–1247, Aug. 2000.

[32] AG Crewell IGMK. (2020). *Instruments Operated by RG Integrated Remote Sensing*. Accessed: Dec. 2020. [Online]. Available: http://gop.meteo.uni-koeln.de/ag_crewell/doku.php?id=instruments:instruments

[33] J. Güldner and D. Spänkuch, "Remote sensing of the thermodynamic state of the atmospheric boundary layer by ground-based microwave radiometry," *J. Atmos. Ocean. Technol.*, vol. 18, no. 6, pp. 925–933, Jun. 2001.

[34] D. Cimini, T. J. Hewison, L. Martin, J. Güldner, C. Gaffard, and F. S. Marzano, "Temperature and humidity profile retrievals from ground-based microwave radiometers during TUC," *Meteorologische Zeitschrift*, vol. 15, no. 1, pp. 45–56, 2006.

[35] S. Crewell and U. Lohnert, "Accuracy of boundary layer temperature profiles retrieved with multifrequency multiangle microwave radiometry," *IEEE Trans. Geosci. Remote Sens.*, vol. 45, no. 7, pp. 2195–2201, Jul. 2007.

[36] U. Löhnert, S. Crewell, and C. Simmer, "An integrated approach toward retrieving physically consistent profiles of temperature, humidity, and cloud liquid water," *J. Appl. Meteorol.*, vol. 43, no. 9, pp. 1295–1307, Sep. 2004. [Online]. Available: https://journals.ametsoc.org/view/journals/apme/43/9/1520-0450_2004_043_1295_aiatrp_2.0.co_2.xml

[37] R. J. Hogan, A. L. M. Grant, A. J. Illingworth, G. N. Pearson, and E. J. O'Connor, "Vertical velocity variance and skewness in clear and cloud-topped boundary layers as revealed by Doppler lidar," *Quart. J. Roy. Meteorol. Soc.*, vol. 135, no. 640, pp. 635–643, Apr. 2009.

[38] G. Pearson, F. Davies, and C. Collier, "Remote sensing of the tropical rain forest boundary layer using pulsed Doppler lidar," *Atmos. Chem. Phys.*, vol. 10, no. 13, pp. 5891–5901, Jul. 2010.

[39] G. N. Pearson and C. G. Collier, "A pulsed coherent CO_2 lidar for boundary-layer meteorology," *Quart. J. Roy. Meteorological Soc.*, vol. 125, no. 559, pp. 2703–2721, Oct. 1999.

[40] C. Flamant, J. Pelon, P. H. Flamant, and P. Durand, "Lidar determination of the entrainment zone thickness at the top of the unstable marine atmospheric boundary layer," *Boundary-Layer Meteorol.*, vol. 83, pp. 247–284, May 1997.

[41] R. Boers and E. W. Eloranta, "Lidar measurements of the atmospheric entrainment zone and the potential temperature jump across the top of the mixed layer," *Boundary-Layer Meteorol.*, vol. 34, no. 4, pp. 357–375, Mar. 1986.

[42] M. de Bruine, A. Apituley, D. P. Donovan, H. Klein Baltink, and M. J. de Haij, "Pathfinder: Applying graph theory to consistent tracking of daytime mixed layer height with backscatter lidar," *Atmos. Meas. Techn.*, vol. 10, no. 5, pp. 1893–1909, May 2017. [Online]. Available: https://amt.copernicus.org/articles/10/1893/2017/

[43] Y. Poltera *et al.*, "PathfinderTURB: An automatic boundary layer algorithm. Development, validation and application to study the impact on *in situ* measurements at the jungfraujoch," *Atmos. Chem. Phys.*, vol. 17, no. 16, pp. 10051–10070, Aug. 2017. [Online]. Available: https://acp.copernicus.org/articles/17/10051/2017/

[44] F. Rocadenbosch, C. Soriano, A. Comerón, and J. Baldasano, "Lidar inversion of atmospheric backscatter and extinction-to-backscatter ratios by use of a Kalman filter," *Appl. Opt.*, vol. 38, no. 15, pp. 3175–3189, 1999.

[45] N. Wiener, *Extrapolation, Interpolation, and Smoothing of Stationary Time Series*. Cambridge, MA, USA: MIT Press, 1964.

[46] R. F. Banks *et al.*, "Sensitivity of boundary-layer variables to PBL schemes in the WRF model based on surface meteorological observations, lidar, and radiosondes during the HygrA-CD campaign," *Atmos. Res.*, vols. 176–177, pp. 185–201, Jul. 2016. [Online]. Available: https://www.sciencedirect.com/science/article/pii/S0169809516300412

[47] R. J. Barlow, *Statistics: A Guide to the Use of Statistical Methods in The Physical Sciences*, R. E. F. Mandl and D. Sandiford, Eds. Chichester, U.K.: Wiley, 1989, ch. 4, pp. 48–67.

[48] K. Reif, S. Günther, E. Yaz, and R. Unbehauen, "Stochastic stability of the discrete-time extended Kalman filter," *IEEE Trans. Autom. Control*, vol. 44, no. 4, pp. 714–728, Apr. 1999.

[49] S. M. Wingo and K. R. Knupp, "Multi-platform observations characterizing the afternoon-to-evening transition of the planetary boundary layer in northern Alabama, USA," *Boundary-Layer Meteorol.*, vol. 155, no. 1, pp. 29–53, Apr. 2015.

[50] M. Haeffelin *et al.*, "Evaluation of mixing-height retrievals from automatic profiling lidars and ceilometers in view of future integrated networks in Europe," *Boundary-Layer Meteorol.*, vol. 143, no. 1, pp. 49–75, Apr. 2012.

[51] D. H. Lenschow, J. C. Wyngaard, and W. T. Pennell, "Mean-field and second-moment budgets in a baroclinic, convective boundary layer," *J. Atmos. Sci.*, vol. 37, no. 6, pp. 1313–1326, Jun. 1980.

[52] S. C. Tucker *et al.*, "Doppler lidar estimation of mixing height using turbulence, shear, and aerosol profiles," *J. Atmos. Ocean. Technol.*, vol. 26, no. 4, pp. 673–688, Apr. 2009.

[53] K. Träumner, C. Kottmeier, U. Corsmeier, and A. Wieser, "Convective boundary-layer entrainment: Short review and progress using Doppler lidar," *Boundary-Layer Meteorol.*, vol. 141, no. 3, pp. 369–391, Dec. 2011.

[54] J. Villalonga *et al.*, "Convective boundary-layer height estimation from combined radar and Doppler lidar observations in VORTEX-SE," in *Remote Sensing of Clouds and the Atmosphere XXV*, vol. 11531, A. Comerón, E. I. Kassianov, K. Schäfer, R. H. Picard, K. Weber, and U. N. Singh, Eds. Bellingham, WA, USA: SPIE, 2020, pp. 192–201, doi: 10.1117/12.2576046.

[55] J. M. Wallace and P. V. Hobbs, *Atmospheric Science: An Introductory Survey*. Amsterdam, The Netherlands: Elsevier, 2006.

[56] D. J. Seidel, C. O. Ao, and K. Li, "Estimating climatological planetary boundary layer heights from radiosonde observations: Comparison of methods and uncertainty analysis," *J. Geophys. Res., Atmos.*, vol. 115, no. D16, pp. D16113-1–D16113-15, 2010. [Online]. Available: https://agupubs.onlinelibrary.wiley.com/doi/full/10.1029/2009JD013680

[57] U. Löhnert and S. Crewell, "Accuracy of cloud liquid water path from ground-based microwave radiometry 1. Dependency on cloud model statistics," *Radio Sci.*, vol. 38, no. 3, pp. 1–11, 2003. [Online]. Available: https://agupubs.onlinelibrary.wiley.com/doi/abs/10.1029/2002RS002654

[58] U. Löhnert, D. D. Turner, and S. Crewell, "Ground-based temperature and humidity profiling using spectral infrared and microwave observations. Part I: Simulated retrieval performance in clear-sky conditions," *J. Appl. Meteorol. Climatol.*, vol. 48, no. 5, pp. 1017–1032, May 2009. [Online]. Available: https://journals.ametsoc.org/view/journals/apme/48/5/2008jamc2060.1.xml

[59] F. Rocadenbosch, R. L. Tanamachi, M. P. Araujo da Silva, J. Villalonga, S. J. Frasier, and D. D. Turner, "Atmospheric boundary layer height disambiguation using synergistic remote sensing observations: Case examples from VORTEX-SE," in *Remote Sensing of Clouds and the Atmosphere XXV*, vol. 11531, A. Comerón, E. I. Kassianov, K. Schäfer, R. H. Picard, K. Weber, and U. N. Singh, Eds. Bellingham, WA, USA: SPIE, 2020, pp. 109–120, doi: 10.1117/12.2576093.

[60] F. Rocadenbosch *et al.*, "Ceilometer-based rain-rate estimation: A case-study comparison with S-band radar and disdrometer retrievals in the context of VORTEX-SE," *IEEE Trans. Geosci. Remote Sens.*, vol. 58, no. 12, pp. 8268–8284, Dec. 2020.

Marcos P. Araújo da Silva (Graduate Student Member, IEEE) received the B.S. degree in environmental engineering and the M.S. degree in climate sciences from the Federal University of Rio Grande do Norte, Natal, Brazil, in 2015 and 2018, respectively. He is pursuing the Ph.D. degree in telecom engineering, remote sensing (advisor, Prof. Francesc Rocadenbosch) with the María-de-Maeztu Excellence Unit CommSensLab-UPC, granted by the Ministerio de Ciencia e Innovación, Spain.

His research interests include atmospheric remote sensing and boundary layer, related multisensor processing, and wind energy.

Francesc Rocadenbosch (Senior Member, IEEE) received the B.S. and Ph.D. degrees in telecommunications engineering from the Universitat Politècnica de Catalunya (UPC), Barcelona, Spain, in 1991 and 1996, respectively, and the M.B.A. degree from the University of Barcelona, Barcelona, in 2001.

In 1993, he joined the Department of Signal Theory and Communications, UPC, where he is a Full Professor. Since 1996, he has been steering the development of CommSensLab-UPC Excellence-Unit activities on lidar, including the UPC unmanned lidar station (European Strategic Forum on Research Infrastructure (ESFRI) 2016 roadmap), and he has been serving on over ten collaborative remote sensing projects as principal investigator (PI). His research interests include remote sensing (lidar-radar-radiometry) for atmospheric observation, related signal processing, and off-shore wind-lidar.

Dr. Rocadenbosch was a recipient of the "Salvà i Campillo" Best Research Project Award in 1997, the National Telecom Award in 2003 (group), and the EU Knowledge and Innovation Communities (KIC) recognition for EOLOS spin-off in 2015. He is an Associate Editor of the IEEE TRANSACTIONS ON GEOSCIENCE AND REMOTE SENSING.

Robin L. Tanamachi received the B.S. degree in atmospheric and oceanic sciences from the University of Wisconsin-Madison, Madison, WI, USA, in 2001, and the M.S. and Ph.D. degrees in meteorology from The University of Oklahoma, Norman, Oklahoma, OK, USA, in 2004 and 2011, respectively.

She is an Assistant Professor with the Department of Earth, Atmospheric, and Planetary Sciences, Purdue University, West Lafayette, IN, USA. Her interests include radar meteorology, severe thunderstorm dynamics and kinematics, and methods for assimilating radar observations into numerical weather prediction models.

Dr. Tanamachi is a member of the American Meteorological Society (AMS) and served on the AMS Radar Meteorology Committee from 2013 to 2019.

Umar Saeed received the B.E. degree in electronics engineering from the National University of Sciences and Technology (NUST), Karachi, Pakistan, in 2007, the M.Sc. degree in communications engineering, with specialization in digital signal processing from Aalto University, Helsinki, Finland, in 2012, and the Ph.D. degree in atmospheric remote sensing from the Universitat Politècnica de Catalunya, Barcelona, Spain, in 2016.

From 2013 to 2016, he was a Marie Curie Early Stage Researcher in the Initial Training for Atmospheric Remote Sensing network funded by the Seventh Framework Program (FP7) of the European Union. His research interests include active optical and passive microwave atmospheric remote sensing, atmospheric boundary layer (BL), sensor synergy, and statistical and adaptive signal processing.